

Diffusion Non-Additive Model for Multi-Fidelity Simulations with Tunable Precision

Junoh Heo, Romain Boutelet and Chih-Li Sung¹²
Michigan State University

Abstract

Computer simulations are indispensable for analyzing complex systems, yet high-fidelity models often incur prohibitive computational costs. Multi-fidelity frameworks address this challenge by combining inexpensive low-fidelity simulations with costly high-fidelity simulations to improve both accuracy and efficiency. However, certain scientific problems demand even more accurate results than the highest-fidelity simulations available, particularly when a tuning parameter controlling simulation accuracy is available, but the exact solution corresponding to a zero-valued parameter remains out of reach. In this paper, we introduce the Diffusion Non-Additive (DNA) model, inspired by generative diffusion models, which captures nonlinear dependencies across fidelity levels using Gaussian process priors and extrapolates to the exact solution. The DNA model: (i) accommodates complex, non-additive relationships across fidelity levels; (ii) employs a nonseparable covariance kernel to model interactions between the tuning parameter and input variables, improving both predictive performance and physical interpretability; and (iii) provides closed-form expressions for the posterior predictive mean and variance, allowing efficient inference and uncertainty quantification. The methodology is validated on a suite of numerical studies and real-world case studies. An R package implementing the proposed methodology is available to support practical applications.

Keywords: Surrogates; Gaussian processes; Finite element methods; Nonseparable kernel; Uncertainty quantification

¹Corresponding author.

²These authors gratefully acknowledge funding from NSF DMS 2338018.

1 Introduction

Computer simulations based on mathematical models have become indispensable for understanding and solving complex engineering and physical problems, particularly when real-world experimentation is costly, hazardous, or infeasible. These simulations often involve models governed by differential equations, which describe various physical phenomena such as heat transfer, structural deformation, electromagnetic fields, and turbulence flows (Mak et al., 2018; Shi et al., 2024; Jin et al., 2025; Sendrea et al., 2024).

Many such simulations incorporate a tuning parameter that controls the trade-off between computational cost and simulation accuracy. A lower value of the tuning parameter corresponds to a higher-fidelity approximation, but typically demands significantly greater computational resources. This setting naturally gives rise to *multi-fidelity modeling*, where data from both inexpensive, low-fidelity simulations and expensive, high-fidelity simulations are used jointly to improve efficiency and predictive performance.

As a concrete example, consider the finite element method (FEM), one of the most widely used numerical methods for solving differential equations in science and engineering (Dhatt et al., 2012). FEM discretizes a complex domain into smaller elements and approximates the governing equations over these elements. The mesh size in FEM serves as the tuning parameter: a finer mesh (i.e., smaller mesh size) improves simulation accuracy by more closely approximating the “true” solution—the numerical result obtained in the limit of zero mesh size (Tuo et al., 2014). Figure 1 illustrates FEM solutions at different mesh sizes, highlighting the impact of discretization on simulation accuracy.

Beyond general FEM solutions, multi-fidelity problems commonly arise in engineering, statistics, mathematics and the sciences, where balancing accuracy against computational cost is a key concern. In signal processing (Clark et al., 2020), for instance, higher sampling rates enhance the precision of signal reconstruction by capturing finer details, yet they require

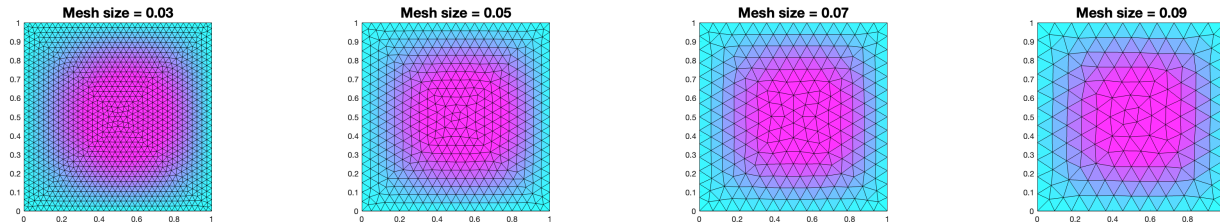


Figure 1: *The visualizations of FEM solutions of the Poisson's equation at $x = 0.5$ for mesh sizes $t = 0.03, 0.05, 0.07,$ and 0.09 .*

greater data storage and processing resources. Optimization problems (Hallmann et al., 2020) exhibit a similar trade-off: tighter convergence tolerances provide more accurate solutions but demand additional iterations and computation time. Bayesian approximation techniques (Li et al., 2014), such as Markov Chain Monte Carlo (MCMC) or Quasi-Monte Carlo, yield more reliable estimates with larger sample sizes, though at an increased computational cost. In time-dependent partial differential equations (de la Hoz and Vellido, 2016), achieving accuracy at a target time T requires simulating from an initial time up to T , with longer simulations incurring proportionally greater expense. Similarly, in hyperparameter optimization for deep learning (Yang et al., 2026), different stopping criteria lead to varying fidelity levels: early stopping results in higher validation loss and lower-fidelity approximations of model performance, while training to full convergence provides high-fidelity estimates at a substantially greater cost.

A wide range of multi-fidelity modeling approaches has been developed in the literature. Notable examples include Kennedy and O'Hagan (2000), Qian et al. (2006), Qian and Wu (2008), Le Gratiet and Garnier (2014), Perdikaris et al. (2017), Kerleguer et al. (2024), and Heo and Sung (2025), along with work on experimental design (Yuchi et al., 2023; Sung et al., 2024) and optimization (Picheny et al., 2013; He et al., 2017). However, most of these methods focus on emulating the highest fidelity simulator available, often without explicitly modeling the tuning parameter that controls fidelity. Exceptions include the work by Tuo et al. (2014), which targets the exact solution in the limit of zero mesh size, as well

as its adaptive kernel extension by Boutelet and Sung (2025) and multi-dimensional tuning parameter generalization by Ji et al. (2024). More recently, Oates et al. (2025) extended Richardson extrapolation within a probabilistic framework, focusing on extrapolating the tuning parameters.

In this paper, we introduce a novel and flexible model, the Diffusion Non-Additive (DNA) model, designed for multi-fidelity data with an associated tuning parameter. The DNA model offers *tunable precision*, meaning it can predict outputs at any specified fidelity level, including extrapolation to the exact solution in the limit as the tuning parameter approaches zero. Inspired by generative diffusion models in deep learning (Ho et al., 2020), the DNA model adopts a recursive structure: lower-fidelity outputs serve as inputs to higher-fidelity levels, and the relationships across fidelities are governed by a Gaussian process (GP) prior. This nonparametric prior enables the model to capture complex, non-additive, and nonlinear dependencies across fidelity levels.

The DNA model offers several key innovations: (i) To the best of our knowledge, it is the first to integrate diffusion-inspired modeling into the multi-fidelity framework. (ii) It employs a nonseparable covariance kernel, drawing on ideas from spatial statistics for spatial-temporal modeling, to model interactions between input variables and the tuning parameter. This not only improves predictive accuracy but also offers interpretable representations of physical relationships. (iii) Although recursive GP structures typically involve computationally intensive procedures (e.g., MCMC) to estimate posterior distributions, we derive closed-form expressions for the posterior mean and variance under nested designs, enabling efficient inference and rigorous uncertainty quantification. (iv) To further enhance modeling flexibility, we extend our approach to fully non-nested experimental designs by developing a stochastic imputation approach for posterior computation.

The organization of this article is as follows. Section 2 introduces the DNA model. Section

3 derives an analytical posterior of the DNA model. In Section 4 and 5, we conduct a comprehensive analysis of various methods through extensive numerical experiments and real-world case studies. Section 6 extends the DNA model to non-nested designs. Finally, Section 7 concludes with a discussion and future directions.

2 DNA Model for Multi-Fidelity Data

2.1 Problem Setup

Let $f(t_l, \mathbf{x})$ represent the scalar simulation output of the computer code with input parameter $\mathbf{x} \in \Omega \subseteq \mathbb{R}^d$ and tuning parameter t_l at fidelity level l . We assume that simulations are conducted at L distinct fidelity levels to train an *emulator* that approximates the true simulator, where a higher fidelity level corresponds to a simulator with more accurate outputs but also higher computational costs per run. The smaller the tuning parameter, the higher the fidelity, such that $t_1 > t_2 > \dots > t_L > 0$.

The primary objective is to construct an efficient emulator for the *exact solution* $f(0, \mathbf{x})$, which corresponds to the limiting case as the tuning parameter approaches zero. Directly evaluating $f(0, \mathbf{x})$ is typically infeasible due to prohibitive computational costs or numerical constraints. For example, in FEM, the tuning parameter corresponds to the mesh size, and achieving the zero limit is often restricted by software resolution capabilities.

For each fidelity level l , simulations are performed at n_l design points, denoted by $\mathcal{X}_l = \{\mathbf{x}_i^{[l]}\}_{i=1}^{n_l}$, at tuning parameter t_l . These simulations yield corresponding outputs $\mathbf{y}_l := \{f(t_l, \mathbf{x})\}_{\mathbf{x} \in \mathcal{X}_l}$, representing the vector of outputs for $f(t_l, \mathbf{x})$ at design points $\mathbf{x} \in \mathcal{X}_l$. Each element of \mathbf{y}_l is denoted by $y_i^{[l]} = f(t_l, \mathbf{x}_i^{[l]})$.

Assume that the designs \mathcal{X}_l are sequentially nested, i.e.,

$$\mathcal{X}_L \subseteq \mathcal{X}_{L-1} \subseteq \cdots \subseteq \mathcal{X}_1 \subseteq \Omega, \quad (1)$$

and $\mathbf{x}_i^{[l]} = \mathbf{x}_i^{[l-1]}$ for $i = 1, \dots, n_l$. In other words, design points for a higher-fidelity simulator are a subset of the design points for a lower-fidelity simulator. This nested design is common in the multi-fidelity modeling literature and has been shown to enable more efficient inference in various approaches (Qian, 2009; Qian et al., 2009; Haaland and Qian, 2010). We extend our approach to accommodate non-nested designs in Section 6.

2.2 Diffusion Non-Additive (DNA) Model

For notational clarity, let $f_l(\mathbf{x}) := f(t_l, \mathbf{x})$. To model the relationship between different fidelity levels, we assume a functional dependence through an unknown function W :

$$\begin{cases} f_1(\mathbf{x}) = W_1(\mathbf{x}), \\ f_l(\mathbf{x}) = W(t_l, \mathbf{x}, f_{l-1}(\mathbf{x})), \quad \text{for } l = 2, \dots, L, \end{cases} \quad (2)$$

where $t_1 > t_2 > \cdots > t_L > 0$. This recursive formulation satisfies the Markov property, as each fidelity level $f_l(\mathbf{x})$ depends only on the immediately preceding level $f_{l-1}(\mathbf{x})$, without direct dependence on earlier levels.

The structure suggests a *diffusion*-like process, where fidelity levels evolve through a recursive relationship. The term “diffusion” is inspired by its analogy in deep learning models (Ho et al., 2020), where similar recursive structures propagate information across layers to enable progressive refinement. Each fidelity level $f_l(\mathbf{x})$ represents the simulator output under a coarser or less accurate configuration such as a relaxed solver tolerance or fewer iterations. As the tuning parameter t_l increases, these choices accumulate approximation error, gradually

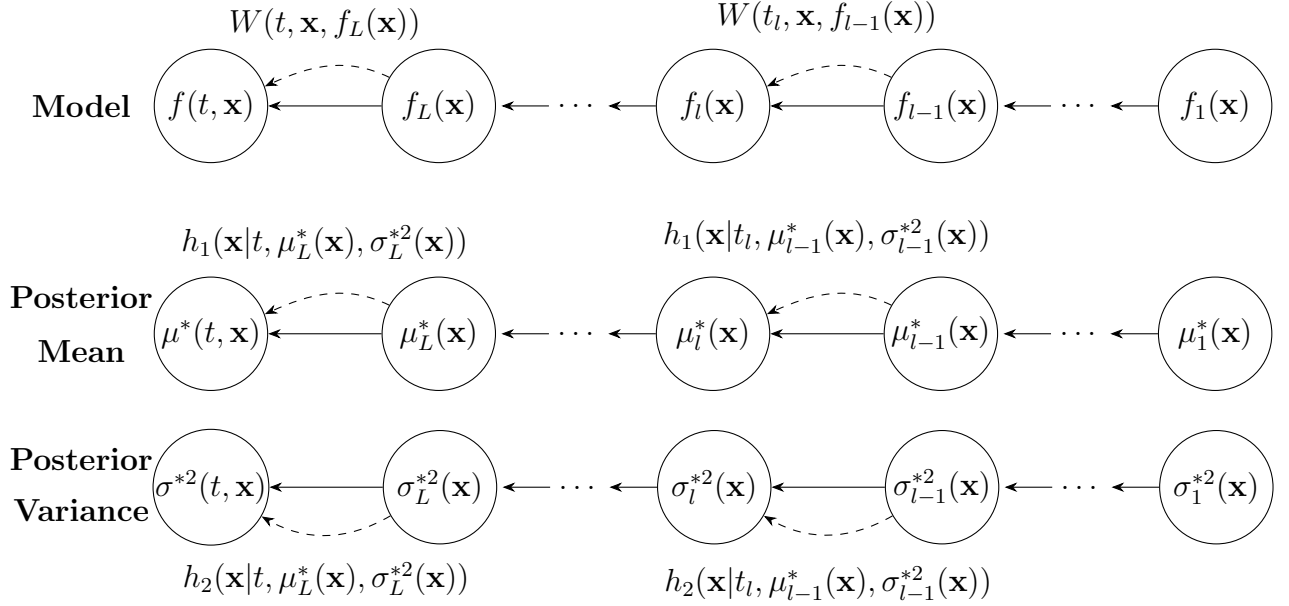


Figure 2: The Markov chain representation of the hierarchical modeling structure, illustrating the relationships between fidelity levels and their corresponding uncertainties. The first row represents the model formulation, where W is assumed to follow a GP prior. The middle and bottom rows present the inference process, showing the posterior mean calculations and posterior variance evaluations, respectively, with h_1 and h_2 having closed-form expressions.

biasing the output away from the exact solution $f(0, \mathbf{x})$ as illustrated in Figure 1. This degradation during the data generation procedure via FEM can be viewed as a *forward diffusion* across fidelity levels. On the other hand, the recursion $f_l(\mathbf{x}) = W(t_l, \mathbf{x}, f_{l-1}(\mathbf{x}))$ exploits this one-step Markov dependence to refine predictions toward $f(0, \mathbf{x})$, resembling a *backward diffusion* process. The hierarchical structure of the model is visualized in the top panel of Figure 2.

Notably, the model proposed in Tuo et al. (2014) assumes $f_l(\mathbf{x}) = f(0, \mathbf{x}) + \delta_l(\mathbf{x})$, which can be interpreted as a special case of the proposed model (2). Specifically, the relationship in (2) can be expressed as:

$$W(t_l, \mathbf{x}, f_{l-1}(\mathbf{x})) = f_{l-1}(\mathbf{x}) + (\delta_l(\mathbf{x}) - \delta_{l-1}(\mathbf{x})),$$

where $\delta_l(\mathbf{x})$ is unknown discrepancy function that converges to 0 as $t_l \rightarrow 0$.

Unlike the additive structure in Tuo et al. (2014), the proposed model (2) is more flexible as it directly incorporates the lower-fidelity output $f_{l-1}(\mathbf{x})$ as an input, allowing for non-additive relationships. This flexibility enables the model to capture complex, non-linear dependencies across fidelity levels. Combining these properties, we name the model the *Diffusion Non-Additive (DNA)* model.

Instead of explicitly specifying W , we model it as a random process using a Gaussian Process (GP) prior (Rasmussen and Williams, 2006; Gramacy, 2020). This GP assumption allows us to flexibly capture complex relationships without overly constraining the model structure. Specifically, we assume:

$$W_1(\mathbf{x}) \sim \mathcal{GP}(\alpha_1, \tau_1^2 K_1(\mathbf{x}, \mathbf{x}')), \quad (3)$$

and

$$W(t, \mathbf{x}, y) \sim \mathcal{GP}(\alpha, \tau^2 K((t, \mathbf{x}, y), (t', \mathbf{x}', y'))), \quad (4)$$

where α_1 and α are a constant mean, τ_1^2 and τ^2 are positive scale parameters, and K_1 and K are positive-definite kernel functions.

The kernel function K_1 can be chosen from commonly used options such as the squared exponential kernel or the Matérn kernel. For instance, the squared exponential kernel is defined as:

$$K_1(\mathbf{x}, \mathbf{x}') = \prod_{j=1}^d \exp\left(-\frac{(x_j - x'_j)^2}{\theta_{1j}}\right), \quad (5)$$

where $(\theta_{11}, \dots, \theta_{1d})$ are the *lengthscale* hyperparameters. For the kernel $K((t, \mathbf{x}, y), (t', \mathbf{x}', y'))$,

we propose the following *nonseparable* formulation:

$$K((t, \mathbf{x}, y), (t', \mathbf{x}', y')) = \left(\frac{(t - t')^2}{\theta_t} + 1 \right)^{-\left(\frac{\beta(d+1)}{2} + \delta\right)} \exp \left(- \left(\frac{(t - t')^2}{\theta_t} + 1 \right)^{-\beta} \left[\frac{(y - y')^2}{\theta_y} + \sum_{j=1}^d \frac{(x_j - x'_j)^2}{\theta_j} \right] \right), \quad (6)$$

where θ_t, θ_y , and $(\theta_1, \dots, \theta_d)$ are the lengthscale parameters. This kernel is inspired by nonseparable spatio-temporal models (Cressie and Huang, 1999; Gneiting, 2002; Porcu et al., 2006; Rodrigues and Diggle, 2010) and is proven to be a valid positive-definite function by Gneiting (2002). Additional discussions on alternative nonseparable kernel functions can be found in Section 7. In this context, the input variables are analogous to spatial coordinates, while the tuning parameter serves as a temporal component.

When $t = t'$, the kernel simplifies to:

$$K((t, \mathbf{x}, y), (t, \mathbf{x}', y')) = \exp \left(- \left(\frac{(y - y')^2}{\theta_y} + \sum_{j=1}^d \frac{(x_j - x'_j)^2}{\theta_j} \right) \right), \quad (7)$$

which resembles conventional kernels based only on input variables, similar to Heo and Sung (2025). Conversely, for $(\mathbf{x}, y) = (\mathbf{x}', y')$, the kernel reduces to:

$$K((t, \mathbf{x}, y), (t', \mathbf{x}, y)) = \left(\frac{(t - t')^2}{\theta_t} + 1 \right)^{-\left(\frac{\beta(d+1)}{2} + \delta\right)}. \quad (8)$$

This expression belongs to the family of *inverse multiquadric* kernels in t and t' (Song and Joseph, 2025), which are generally written as $K(t, t') = \left(\frac{(t - t')^2}{\theta} + 1 \right)^{-\nu}$, where ν is the smoothness parameter.

The covariance kernel $K((t, \mathbf{x}, y), (t', \mathbf{x}', y'))$ is nonseparable, meaning that it cannot be decomposed into the sum or the product of a purely input kernel (7) and a purely tuning parameter kernel (8). This coupling allows the model to modulate the interaction between

(\mathbf{x}, y) and the tuning parameter t , with the parameter $0 \leq \beta \leq 1$ playing a key role in governing this interaction. As β increases, the coupling becomes stronger, and the correlation between (\mathbf{x}, y) and (\mathbf{x}', y') decays more quickly when the tuning parameters t and t' differ. Importantly, when $\beta = 0$, meaning there is no interaction between the tuning parameter and the inputs, the kernel simplifies to a separable form:

$$K((t, \mathbf{x}, y), (t, \mathbf{x}', y')) = \left(\frac{(t - t')^2}{\theta_t} + 1 \right)^{-\delta} \exp \left(- \left(\frac{(y - y')^2}{\theta_y} + \sum_{j=1}^d \frac{(x_j - x'_j)^2}{\theta_j} \right) \right),$$

making the separable kernel a special case of the proposed kernel function.

Remark 2.1. The requirement $\delta > 0$ not only controls the baseline decay in t , ensuring that the effects of the tuning parameters remain non-negligible, but also improves numerical stability by enhancing the conditioning of the kernel matrix. To illustrate this, consider the condition number $\kappa(\mathbf{K})$, defined as the ratio of the largest to smallest eigenvalue of the kernel matrix \mathbf{K} . A large condition number indicates that the matrix is nearly singular, which can cause numerical instability in matrix inversion or Cholesky decomposition. Consider a simplified case with tuning parameters t_1, \dots, t_L and common input locations $\mathcal{X} := \mathcal{X}_1 = \dots = \mathcal{X}_L$. Suppose $\theta_y \rightarrow \infty$ and $\beta = 0$. For the kernel matrix \mathbf{K} constructed from equation (6), it can be shown that, when $\delta = 0$, the condition number $\kappa(\mathbf{K}) = \infty$, indicating that the matrix is numerically ill-conditioned. In contrast, when $\delta > 0$, the condition number $\kappa(\mathbf{K}) < \infty$, implying improved numerical behavior. A formal proof of this result is provided in Supplementary Materials S1. Based on this, we impose a lower bound of 0.5 on δ during parameter estimation.

It is also worth noting that, unlike the recent Recursive Non-Additive (RNA) model (Heo and Sung, 2025) and the nonlinear auto-regressive GP model (Perdikaris et al., 2017), which constructs a separate GP at each fidelity level l with its own hyperparameters, the

DNA model incorporates the tuning parameter t_l as an additional input and embeds all non-lowest-fidelity outputs into a single GP. By augmenting the input space to (t, \mathbf{x}, y) , DNA employs a shared lengthscale and scale parameter across levels $2, \dots, L$, reducing the total number of lengthscale hyperparameters from $(dL + L - 1)$ in RNA to $(2d + 1)$. Moreover, the explicit inclusion of t facilitates DNA to perform direct inference for higher-fidelity outputs (i.e., extrapolation to smaller tuning parameters and even the exact solution, i.e., $t = 0$).

2.3 Parameter Estimation

The proposed model involves several unknown parameters, including the mean parameters α_1, α , the lengthscale parameters $\{\theta_{1j}\}_{j=1}^d, \{\theta_j\}_{j=1}^d, \theta_y$, and θ_t , scale parameters τ_1^2 and τ^2 , the interaction parameter β , and the smoothness parameter δ . These parameters are estimated using the maximum likelihood estimation (MLE) method. Specifically, under the GP assumption for $W_1(\mathbf{x})$ in (3), it follows that:

$$\mathbf{y}_1 \sim \mathcal{N}(\alpha_1 \mathbf{1}_{n_1}, \tau_1^2 \mathbf{K}_1),$$

where \mathbf{K}_1 is an $n_1 \times n_1$ matrix with elements $(\mathbf{K}_1)_{ij} = K_1(\mathbf{x}_i^{[1]}, \mathbf{x}_j^{[1]})$. Similarly, under the DNA model (4), the observed simulations $(\mathbf{y}_2^T, \dots, \mathbf{y}_L^T)^T$ follow a multivariate normal distribution:

$$Y_{-1} := \begin{bmatrix} \mathbf{y}_2 \\ \vdots \\ \mathbf{y}_L \end{bmatrix} \sim \mathcal{N}_{N_{-1}}(\alpha \mathbf{1}_{N_{-1}}, \tau^2 \mathbf{K}),$$

where $N_{-1} = \sum_{l=2}^L n_l$, \mathbf{K} is an $N_{-1} \times N_{-1}$ matrix with elements

$$\mathbf{K}_{ij} = K(((\mathbf{t}_{-1})_i, (\mathbf{X}_{-1})_i, (Y_{-L})_i), ((\mathbf{t}_{-1})_j, (\mathbf{X}_{-1})_j, (Y_{-L})_j)),$$

and $\mathbf{X}_{-1} = (\mathcal{X}_2^T, \dots, \mathcal{X}_L^T)^T$, $\mathbf{t}_{-1} = (t_2 \mathbf{1}_{n_2}^T, \dots, t_L \mathbf{1}_{n_L}^T)^T$, and $Y_{-1} = (\mathbf{y}_1[1 : n_2]^T, \mathbf{y}_2[1 : n_3]^T, \dots, \mathbf{y}_{L-1}[1 : n_L]^T)^T$, where $\mathbf{y}_l[1 : n_k]$ denotes the first n_k samples of \mathbf{y}_l . The MLE estimates for $\alpha_1, \alpha, \tau_1^2$ and τ^2 are given by

$$\hat{\alpha}_1 = \frac{\mathbf{y}_1^T \mathbf{K}_1^{-1} \mathbf{y}_1}{\mathbf{1}_{n_1}^T \mathbf{K}_1^{-1} \mathbf{1}_{n_1}}, \quad \hat{\alpha} = \frac{Y_{-1}^T \mathbf{K}^{-1} Y_{-1}}{\mathbf{1}_{N-1}^T \mathbf{K}^{-1} \mathbf{1}_{N-1}},$$

and

$$\hat{\tau}_1^2 = \frac{(\mathbf{y}_1 - \hat{\alpha}_1 \mathbf{1}_{n_1})^T \mathbf{K}_1^{-1} (\mathbf{y}_1 - \hat{\alpha}_1 \mathbf{1}_{n_1})}{n_1}, \quad \hat{\tau}^2 = \frac{(Y_{-1} - \hat{\alpha} \mathbf{1}_{N-1})^T \mathbf{K}^{-1} (Y_{-1} - \hat{\alpha} \mathbf{1}_{N-1})}{N-1}.$$

The remaining kernel parameters associated with K are estimated by maximizing the profile log-likelihood (up to an additive constant):

$$-\frac{1}{2} \log(\det(\mathbf{K})) + \frac{N-1}{2} \log \left((Y_{-1} - \hat{\alpha} \mathbf{1}_{N-1})^T \mathbf{K}^{-1} (Y_{-1} - \hat{\alpha} \mathbf{1}_{N-1}) \right). \quad (9)$$

These parameters can be efficiently estimated using optimization algorithms such as the quasi-Newton method (Byrd et al., 1995). A similar MLE approach is used to estimate the parameters associated with K_1 . The gradient of the log-likelihood, provided in the Supplementary Materials S2, has a closed-form expression, which facilitates faster and more stable convergence.

3 Posterior of DNA Model

In this section, we derive the posterior distribution of $f(t, \mathbf{x})$ for $0 \leq t < t_L$ and $\mathbf{x} \in \Omega$, given the observations $Y_N := \{\mathbf{y}_l\}_{l=1}^L$, where $N = \sum_{l=1}^L n_l$. Due to the complex non-additive relationship in (2) and the GP prior, computing the posterior can be computationally

demanding, often requiring numerical techniques such as Monte Carlo integration. To address this, we derive the closed-form expressions for the posterior mean and variance in a recursive manner, which significantly improves computational efficiency.

By the GP assumptions, the posterior distribution of f_l given Y_N and f_{l-1} at a new input location \mathbf{x} is normally distributed. Specifically, for $l = 1$, we have:

$$W_1(\mathbf{x})|\mathbf{y}_1 \sim \mathcal{N}(\mu_1(\mathbf{x}), \sigma_1^2(\mathbf{x})), \quad (10)$$

with

$$\mu_1(\mathbf{x}) = \alpha_1 + \mathbf{k}_1(\mathbf{x})^T \mathbf{K}_1^{-1}(\mathbf{y}_1 - \alpha_1 \mathbf{1}_{n_1}), \quad \text{and} \quad (11)$$

$$\sigma_1^2(\mathbf{x}) = \tau_1^2 (1 - \mathbf{k}_1(\mathbf{x})^T \mathbf{K}_1^{-1} \mathbf{k}_1(\mathbf{x})), \quad (12)$$

where $\mathbf{k}_1(\mathbf{x})$ is an $n_1 \times 1$ matrix with elements $(\mathbf{k}_1(\mathbf{x}))_{i,1} = K_1(\mathbf{x}, \mathbf{x}_i^{[1]})$.

For $l \geq 2$, the posterior distribution of $f_l(\mathbf{x})$ is:

$$f_l(\mathbf{x})|Y_N, f_{l-1}(\mathbf{x}) \sim \mathcal{N}(\mu_l(\mathbf{x}, f_{l-1}(\mathbf{x})), \sigma_l^2(\mathbf{x}, f_{l-1}(\mathbf{x}))),$$

with

$$\mu_l(\mathbf{x}, f_{l-1}(\mathbf{x})) = \alpha + \mathbf{k}(t_l, \mathbf{x}, f_{l-1}(\mathbf{x}))^T \mathbf{K}^{-1}(Y_{-1} - \alpha \mathbf{1}_{N-1}), \quad \text{and} \quad (13)$$

$$\sigma_l^2(\mathbf{x}, f_{l-1}(\mathbf{x})) = \tau^2 (1 - \mathbf{k}(t_l, \mathbf{x}, f_{l-1}(\mathbf{x}))^T \mathbf{K}^{-1} \mathbf{k}(t_l, \mathbf{x}, f_{l-1}(\mathbf{x}))), \quad (14)$$

where $\mathbf{k}(t_l, \mathbf{x}, f_{l-1}(\mathbf{x}))$ is an $N_{-1} \times 1$ matrix with elements:

$$(\mathbf{k}(t_l, \mathbf{x}, f_{l-1}(\mathbf{x})))_{i,1} = K((t_l, \mathbf{x}, f_{l-1}(\mathbf{x})), ((\mathbf{t}_{-1})_i, (\mathbf{X}_{-1})_i, (Y_{-L})_i)).$$

Similarly, for $0 \leq t < t_L$, the posterior distribution of $f(t, \mathbf{x})$ given Y_N and $f_L(\mathbf{x})$ is:

$$f(t, \mathbf{x})|Y_N, f_L(\mathbf{x}) \sim \mathcal{N}(\mu_{L+1}(t, \mathbf{x}, f_L(\mathbf{x})), \sigma_{L+1}^2(t, \mathbf{x}, f_L(\mathbf{x}))),$$

with

$$\begin{aligned} \mu_{L+1}(t, \mathbf{x}, f_L(\mathbf{x})) &= \alpha + \mathbf{k}(t, \mathbf{x}, f_L(\mathbf{x}))^T \mathbf{K}^{-1} (Y_{-1} - \alpha \mathbf{1}_{N_{-1}}), \\ \sigma_{L+1}^2(t, \mathbf{x}, f_L(\mathbf{x})) &= \tau^2 (1 - \mathbf{k}(t, \mathbf{x}, f_L(\mathbf{x}))^T \mathbf{K}^{-1} \mathbf{k}(t, \mathbf{x}, f_L(\mathbf{x}))). \end{aligned}$$

The posterior distribution of $f(t, \mathbf{x})$ for $0 \leq t < t_L$ can then be expressed as:

$$\begin{aligned} p(f(t, \mathbf{x})|Y_N) &= \int \cdots \int p(f(t, \mathbf{x})|Y_N, f_L(\mathbf{x})) p(f_L(\mathbf{x})|Y_N, f_{L-1}(\mathbf{x})) p(f_{L-1}(\mathbf{x})|Y_N, f_{L-2}(\mathbf{x})) \cdots \\ &\quad p(f_2(\mathbf{x})|Y_N, f_1(\mathbf{x})) p(f_1(\mathbf{x})|Y_N) df_L(\mathbf{x}) \cdots df_1(\mathbf{x}). \end{aligned}$$

While each component p is a normal distribution, evaluating this integral directly can be computationally expensive, especially when L is large. To address this, we extend the approach of Heo and Sung (2025) and derive the posterior mean and variance in a closed-form recursive fashion, as stated in the following proposition.

Proposition 3.1. *Under the kernel functions (5) and (6), the posterior mean and variance of $f(t, \mathbf{x})$ given the data Y_N for $0 \leq t < t_L$ can be expressed in a recursive fashion:*

$$\begin{aligned} \mu^*(t, \mathbf{x}) &= \mathbb{E}[f(t, \mathbf{x})|Y_N] = h_1(\mathbf{x}|t, \mu_L^*(\mathbf{x}), \sigma_L^{*2}(\mathbf{x})), \\ \sigma^{*2}(t, \mathbf{x}) &= \mathbb{V}[f(t, \mathbf{x})|Y_N] = h_2(\mathbf{x}|t, \mu_L^*(\mathbf{x}), \sigma_L^{*2}(\mathbf{x})), \end{aligned}$$

and for $l = 2, \dots, L$,

$$\mu_l^*(\mathbf{x}) = \mathbb{E}[f_l(\mathbf{x})|Y_N] = h_1(\mathbf{x}|t_l, \mu_{l-1}^*(\mathbf{x}), \sigma_{l-1}^{*2}(\mathbf{x})),$$

$$\sigma_l^{*2}(\mathbf{x}) = \mathbb{V}[f_l(\mathbf{x})|Y_N] = h_2(\mathbf{x}|t_l, \mu_{l-1}^*(\mathbf{x}), \sigma_{l-1}^{*2}(\mathbf{x})),$$

where

$$h_1(\mathbf{x}|t, \mu, \sigma^2) = \alpha + \sqrt{\frac{\theta_y}{\theta_y + 2\sigma^2}} \sum_{i=1}^{N-1} r_i c_i^{\frac{d+1}{2} + \frac{\delta}{\beta}} \exp\left(-c_i \left\{ \sum_{j=1}^d \frac{(x_j - (\mathbf{X}_{-1})_{ij})^2}{\theta_j} + \frac{((Y_{-L})_i - \mu)^2}{\theta_y + 2\sigma^2} \right\}\right)$$

and

$$h_2(\mathbf{x}|t, \mu, \sigma^2) = \tau^2 - (\mu - \alpha)^2 + \left(\sum_{i,k=1}^{N-1} \zeta_{ik}(t, \mu, \sigma^2) (r_i r_k - \tau^2 (\mathbf{K}^{-1})_{ik}) (c_i c_k)^{\frac{d+1}{2} + \frac{\delta}{\beta}} \right) \\ \times \exp\left(-\sum_{j=1}^d \frac{c_i (x_j - (\mathbf{X}_{-1})_{ij})^2 + c_k (x_j - (\mathbf{X}_{-1})_{kj})^2}{\theta_j}\right),$$

where $r_i = (\mathbf{K}^{-1}(Y_{-1} - \alpha \mathbf{1}_{N-1}))_i$, $c_i := c(t, \mathbf{t}_i) = \left(\frac{(t - \mathbf{t}_i)^2}{\theta_t} + 1\right)^{-\beta}$ and

$$\zeta_{ik}(t, \mu, \sigma^2) = \sqrt{\frac{\theta_y}{\theta_y + 2(c_i + c_k)\sigma^2}} \\ \times \exp\left(-\frac{c_i ((Y_{-L})_i - \mu)^2 + c_k ((Y_{-L})_k - \mu)^2 + \frac{2}{\theta_y} c_i c_k \sigma^2 ((Y_{-L})_i - (Y_{-L})_k)^2}{\theta_y + 2(c_i + c_k)\sigma^2}\right).$$

For $l = 1$, it follows that $\mu_1^*(\mathbf{x}) = \mu_1(\mathbf{x})$ and $\sigma_1^{*2}(\mathbf{x}) = \sigma_1^2(\mathbf{x})$ as in (11) and (12), respectively.

The full derivations for Proposition 3.1 are provided in Supplementary Materials S3. While the nonseparable kernel in (6) is based on the squared exponential kernel, we also develop a nonseparable variant based on the Matérn kernel (Stein, 1999), another widely used choice. Supplementary Materials S4 includes this alternative kernel and its closed-form

expressions for the posterior mean and variance are provided in Supplementary Materials S5. These derivations build on the work of Kyzyurova et al. (2018), Ming and Guillas (2021), and Heo and Sung (2025).

Proposition 3.1 enables efficient computation of the posterior mean and variance through a recursive formulation. The hierarchical structure of the posterior inference process is illustrated in Figure 2. To approximate the posterior distribution, we adopt the *moment-matching* method, leveraging the Gaussian approximation based on the derived posterior mean and variance. This Gaussian approximation to the DNA model minimizes the Kullback–Leibler divergence between the true distribution and its Gaussian representation (Minka, 2001). The unknown parameters in the posterior distribution are replaced by their corresponding estimates. An R package, `DNAmf`, implementing the proposed methods is available on an open repository.

4 Numerical Studies

In this section, we evaluate the proposed model on four synthetic functions, each designed to test a different form of multi-fidelity dependence. The functions are defined as follows:

$$\left\{ \begin{array}{l} f(t, x) = \exp(-1.4x) \cos(3.5\pi x) + t^2 \sin(40x)/10, \quad x \in [0, 1], \\ f(t, x) = \sin\left(\frac{10\pi x}{5+t}\right) + 0.2 \sin(8\pi x), \quad x \in [0, 1], \\ f(t, \mathbf{x}) = \left[\exp(-4t) - \exp\left(-\frac{1}{2x_2}\right) \right] \frac{2300x_1^3 + 1900x_1^2 + 2092x_1 + 60}{100x_1^3 + 500x_1^2 + 4x_1 + 20}, \quad \mathbf{x} = (x_1, x_2) \in [0, 1]^2. \\ f(t, \mathbf{x}) = \frac{(2\pi - t^2)T_u(H_u - H_l)}{\log(r/r_w) \left(1 + t^2 + \frac{2LT_u}{\log(r/r_w)r_w^2 K_w} + \frac{T_u}{T_l} \right)}, \end{array} \right.$$

where $r_w \in [0.05, 0.15]$, $r \in [100, 50000]$, $T_u \in [63070, 115600]$, $H_u \in [990, 1110]$, $T_l \in [63.1, 116]$, $H_l \in [700, 820]$, $L \in [1120, 1680]$, and $K_w \in [9855, 12045]$. The first one-

dimensional function is from Tuo et al. (2014), which exhibits an additive structure (referred to as the additive function) and yields the exact solution $f(0, x) = \exp(-1.4x) \cos(3.5\pi x)$. The second function is adapted from Higdon (2002) (referred to as the non-additive function), where t is in the denominator, showing a nonlinear relationship between different tuning parameters. The third synthetic example is the multi-fidelity Currin function (Currin, 1988) from Sung et al. (2024). The last synthetic example is the multi-fidelity Borehole function adapted from Xiong et al. (2013).

The tuning parameter t_l is chosen using a systematic refinement approach. Specifically, a geometric refinement is employed such that $t_l = ct_{l-1}$ with a constant ratio $c < 1$, ensuring proportional reduction of the discretization spacing across levels. In scientific computing, such geometric refinement serves as a fundamental component in assessing the observed order of accuracy and the Grid Convergence Index, which formally verifies numerical convergence and quantifies discretization uncertainty (Oberkampf and Roy, 2025). In the present numerical studies, we set $c = 0.7$. The choice of sample sizes follows a similar geometric relation, given by $n_{l-1} = \lfloor c^{-\gamma} n_l \rfloor$, where $\gamma = 2$, which maintains a consistent balance between the refinement of the tuning parameter and the allocation of sample sizes across levels. Additional results under different choices of c and γ are provided in supplementary materials S7. The input locations are generated from the nested space-filling design introduced by Le Gratiet and Garnier (2014), with the largest tuning parameter t_L given in the last column of Table 1, which also summarizes the sample sizes and input dimensions for each function.

	n_1	n_2	n_3	n_4	n_5	n_6	d	t_L
Additive	17	8	4	2	1		1	2.5
Non-additive	17	8	4	2	1		1	2.5
Currin	71	35	17	8	4	2	2	2.5
Borehole	71	35	17	8	4	2	8	2.5

Table 1: Sample sizes n_l , input dimension d , and the largest tuning parameter t_L for each synthetic example.

We compare the predictive performance of the proposed model (labeled **DNAmf**) with four existing methods: two that aim to emulate highest fidelity output $f(t_L, \mathbf{x})$, including the Recursive Non-Additive emulator (**RNAmf**) by Heo and Sung (2025) and the auto-regressive model (**CoKriging**) by Le Gratiet and Garnier (2014), and the nonlinear auto-regressive GP model (**NARGP**) by Perdikaris et al. (2017). The remaining two methods target the exact solution $f(0, \mathbf{x})$, namely the nonstationary GP model by Tuo et al. (2014) using Brownian motion kernel function (**BM**), and its extension using fractional Brownian motion kernel function (**FBM**) proposed by Boutelet and Sung (2025). Due to structural limitations, the **RNAmf**, **CoKriging**, and **NARGP** models are restricted to using only three fidelity levels ($l = 1, 2, 3$ for the additive, non-additive, and Borehole functions, and $l = 3, 4, 5$ for the Currin function).

The model performance is evaluated using the root-mean-square error (RMSE) and continuous rank probability score (CRPS) (Gneiting and Raftery, 2007), which accounts for the predictive distribution (including the mean and variance), based on 100 test points uniformly sampled from the same input space. Lower RMSE and CRPS values indicate better model accuracy.

Figure 3 illustrates model predictions along with confidence intervals for the additive and non-additive functions across different values of the tuning parameter t . By assuming that each fidelity level depends only on the immediately preceding level, the model effectively captures the evolving relationship as t decreases to 0. Notably, the model accurately predicts the function at $t = 0$ despite the absence of design points at this value. The confidence intervals mostly contain the true function, demonstrating the effectiveness of the uncertainty quantification. This extrapolation capability demonstrates the model’s practical utility in situations where data at very small values of t are unavailable, which reduces the need for costly data collection while maintaining predictive accuracy.

Figure 4 shows RMSE and CRPS results across 100 independent repetitions, each using randomly selected training input locations. The proposed DNAmf method consistently outperforms all four competing methods in both metrics. Even for the additive function, DNAmf still achieves superior performance. For the non-additive and Currin functions, where

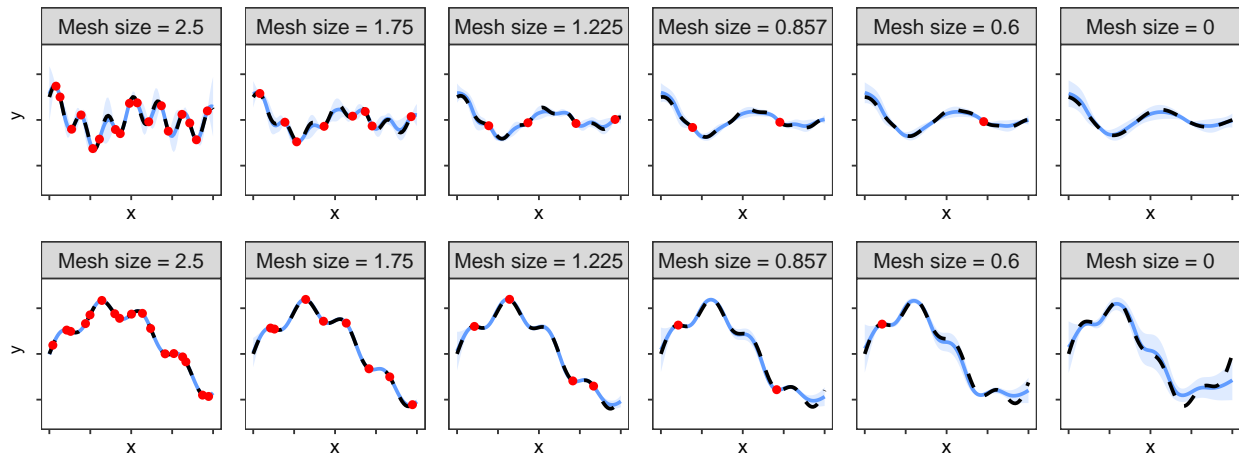


Figure 3: Illustrations of the additive function (top row) and the non-additive function (bottom row). Each row consists of subplots with tuning parameter values decreasing from large (left) to zero (right). In each subplot, the black dashed line represents the true function, red dots denote the design points, the blue line indicates the predicted function, and the shaded region depicts the 99% confidence interval.

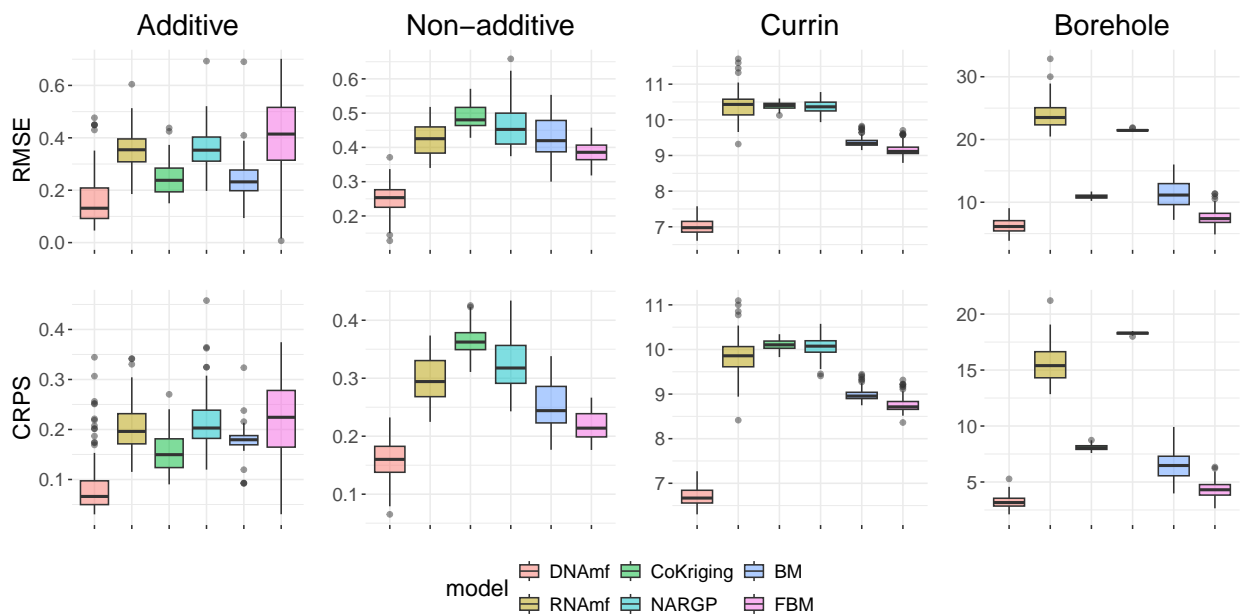


Figure 4: RMSEs and CRPSs of four synthetic examples across 100 repetitions.

the tuning parameter t influences the output nonlinearly, the model’s flexible structure leads to substantially greater improvements. For the Borehole function, DNAmf and FBM achieve the best performance among all methods, demonstrating the effectiveness of DNAmf in high-dimensional settings.

Notably, RNAmf, CoKriging, and NARGP show relatively suboptimal performance. This is because they fit separate GPs at each fidelity level, relying only on the limited design points available at that level. As a result, they cannot utilize the highest fidelity level in the additive and non-additive functions, where only a single output is available. Furthermore, these methods focus solely on emulating the highest fidelity output $f(t_L, \mathbf{x})$, without extrapolating to $f(0, \mathbf{x})$. In contrast, DNAmf, BM, and FBM leverage all available data across fidelity levels to build a unified emulator capable of extrapolation. This ability to pool information leads to better predictive performance, particularly when each level has a limited number of design points.

The proposed model also offers interpretability through the parameter β , which captures the strength of interaction between \mathbf{x} and t . For the non-additive function, a stronger coupling is observed, reflected in a higher average estimated interaction parameter $\hat{\beta} = 0.007$, in contrast to $\hat{\beta} = 0$ for the additive, Currin, and Borehole function.

5 Real Applications

In this section, we present three case studies to evaluate the predictive performance of the proposed approach in scenarios where obtaining an exact solution within a finite time or cost is infeasible or difficult. Simulations are conducted at five fidelity levels, corresponding to five different mesh resolutions. As in Section 4, the designs are generated using the nested space-filling design of Le Gratiet and Garnier (2014).

The three case studies are introduced below:

- **Poisson’s Equation:** Elliptic PDEs commonly appear in the modeling of many physical phenomena. Specifically, we examine Poisson’s equation (Evans, 2010; Tuo et al., 2014; Sung et al., 2024) on the square domain $\Omega = [0, 1]^2$, defined as follows:

$$\Delta u = (x^2 - 2\pi^2) e^{xs_1} \sin(\pi s_1) \sin(\pi s_2) + 2x\pi e^{xs_1} \cos(\pi s_1) \sin(\pi s_2), \quad \mathbf{s} = (s_1, s_2) \in \Omega,$$

where $x \in [-1, 1]$ is the one-dimensional input variable, $\Delta = \frac{\partial^2}{\partial x^2} + \frac{\partial^2}{\partial y^2}$ is the Laplace operator, and Ω represents a square membrane. The Dirichlet boundary condition $u = 0$ is imposed on the boundary $\partial\Omega$. Our quantity of interest is the maximum of u over Ω , which captures the highest stress or displacement of the membrane. Poisson’s equation admits the known analytical solution at any given $x \in [-1, 1]$ and point $(s_1, s_2) \in \Omega$ as $u(s_1, s_2; x) = e^{xs_1} \sin(\pi s_1) \sin(\pi s_2)$, which allows us to evaluate the performance of the model in approximating the exact solution $f(0, x)$. For each combination of x and the mesh size t , we solve the PDE via finite element simulations using the **Partial Differential Equation Toolbox** of MATLAB (MATLAB., 2021), as illustrated in Figure 1.

- **Vibration of Square Plate:** The second case study focuses on the fourth natural frequencies in hertz (Hz) of a square elastic plate of size $10 \times 10 \times 1$ (Li et al., 2020). Three material properties serve as input variables: Young’s modulus ($x_1 \in [1 \times 10^{11}, 4 \times 10^{11}]$), Poisson’s ratio ($x_2 \in [0.2, 0.4]$), and mass density ($x_3 \in [6 \times 10^3, 9 \times 10^3]$). Fidelity is again controlled by the finite-element mesh size t (see Figure 5). Because an analytical solution for the plate’s frequencies at infinite resolution is unavailable and high-resolution simulations are computationally expensive, we treat $t = 0.3$ as the finest mesh for evaluating model performance. Simulations at this resolution are conducted at 100 uniform test input locations, with each run taking up to 8 minutes. The frequencies

are computed via FEM using MATLAB.

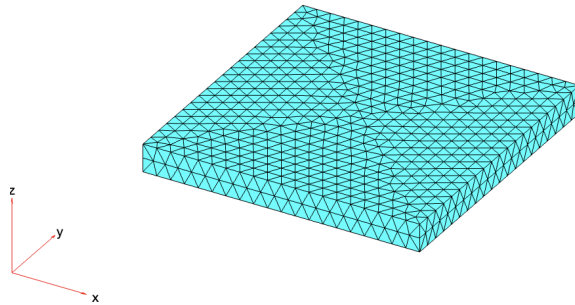


Figure 5: *Illustration of the FEM mesh generation with the maximum mesh edge length $t = 0.5$ for mechanical plate.*

- **Heat Equation:** In the multi-fidelity framework, a time-dependent parabolic PDE can be viewed as a hierarchy of models indexed by their temporal proximity to the target time S . We consider a one-dimensional heat equation, a canonical instance of the diffusion equation:

$$\frac{\partial u(x, s)}{\partial s} = D \frac{\partial^2 u(x, s)}{\partial x^2},$$

where $u(x, s)$ denotes the temperature at spatial coordinate $x \in [0, L]$ and time $s \in [0, S]$, and D denotes the thermal diffusivity coefficient. As s approaches the target time S , the solution generally exhibits increasing complexity both in its spatial gradients and in the coupling between space and time. Consequently, direct integration from $s = 0$ to $s = S$ on a fine time grid can become prohibitive. To address this, we introduce the tuning parameter $t = S - s$ that measures the temporal distance from the simulation time s to the target time S . Early time-step solutions, (i.e., larger t , smaller s) provide inexpensive, low-fidelity information, while those obtained closer to the target time (i.e., smaller t , larger s) yield high-fidelity results at greater cost. To evaluate model performance, we compute the exact solution at $t = 0$ at 100 uniform test input locations.

As in Section 4, model performance is evaluated using the RMSE and CRPS on 100 test

points with 100 repetitions. The sample sizes, input dimensions, the largest value of the tuning parameters, and constant ratio c for each case study are summarized in Table 2. These mesh sizes and sample sizes are chosen in a similar fashion as in Section 4.

	n_1	n_2	n_3	n_4	n_5	d	t_L	c
Poisson	17	11	7	5	3	1	0.1	0.65
Plate	28	21	15	11	8	3	0.55	0.9
Heat	25	15	9	5	3	1	0.5	0.7

Table 2: Sample sizes n_l , input dimension d , the largest tuning parameter t_L , and the constant c that determines the other tuning parameters, $t_l = ct_{l-1}$, for each case study.

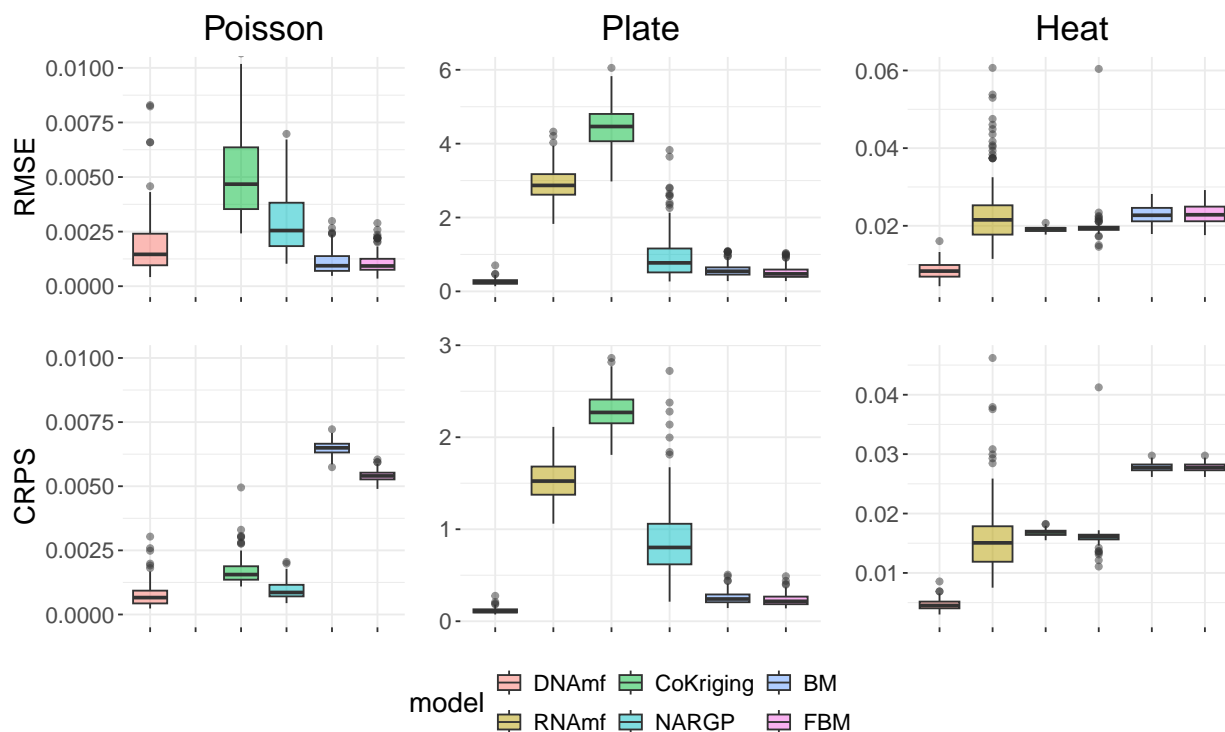


Figure 6: RMSEs and CRPSs of three real case studies across 100 repetitions.

As shown in Figure 6, DNAmf generally outperforms all other competitors across all case studies, with the exception of RMSE in the Poisson equation, where it is slightly less accurate than both FBM and BM. However, DNAmf achieves better CRPS in that case, indicating improved uncertainty quantification. Notably, RNAmf performs considerably worse for the Poisson equation, with both RMSE and CRPS values exceeding the displayed range in

Figure 6. This degraded performance likely stems from its structural limitation of fitting separate GPs at each fidelity level using relatively few design points, which restricts its ability to effectively capture cross-level dependencies. The estimated interaction parameter $\hat{\beta}$ and the visualizations in Figure S5 together highlight differences in coupling behavior. For both the Poisson and Plate problems, $\hat{\beta} \approx 0$, suggesting that the kernel becomes effectively separable. This indicates that the influence of the input variables remains nearly constant across different values of the tuning parameter t , which is consistent with the top row of Figure S5, where model predictions and confidence intervals show little variation over t . In contrast, for the Heat equation, $\hat{\beta} \approx 1$, revealing the pronounced interaction between inputs and the fidelity level. This behavior is also evident in the bottom row of Figure S5, where the predictive results vary substantially with t , clearly reflecting the strong interaction between the input variables and tuning parameter captured by the nonseparable kernel.

6 DNA Model with Non-Nested Design

While the nested structure in (1) enables an efficient DNA model, it is not always applicable or available in practice. In this section, we extend our framework to accommodate non-nested designs while preserving computational efficiency by leveraging the developments in Sections 2 and 3.

To achieve this, we adopt the stochastic imputation approach proposed by Ming et al. (2023). Specifically, we impute *pseudo* outputs at chosen *pseudo* inputs to construct an artificial nested design, allowing us to retain the efficient computation of the DNA model.

Let $\mathcal{X}_L^* = \mathcal{X}_L$ and $\mathcal{X}_l^* = \mathcal{X}_l \cup \mathcal{X}_{l+1}^*$ for $l = 1, \dots, L - 1$. Assume that $\mathcal{X}_l \cap \mathcal{X}_{l+1} = \emptyset$. Under this construction, the resulting design satisfies the nested structure:

$$\mathcal{X}_L^* \subseteq \mathcal{X}_{L-1}^* \subseteq \dots \subseteq \mathcal{X}_1^* \subseteq \Omega.$$

Denote the *pseudo* inputs as $\tilde{\mathcal{X}}_l := \mathcal{X}_l^* \setminus \mathcal{X}_l$, their corresponding *pseudo* outputs are given by $\tilde{\mathbf{y}}_l := f_l(\tilde{\mathcal{X}}_l)$. Furthermore, we define \mathbf{y}_l^* as the combined output, incorporating both the original and *pseudo* outputs: $\mathbf{y}_l^* = f_l(\mathcal{X}_l^*)$.

6.1 Estimation

We first focus on estimating the unknown parameters $\varphi = (\alpha_1, \alpha, \tau_1^2, \tau^2, \beta, \delta, \boldsymbol{\theta})$ where $\boldsymbol{\theta} = (\{\theta_j\}_{j=1}^d, \theta_y, \theta_t)$, for which we employ the stochastic expectation-maximization (SEM) method (Celeux and Diebolt, 1985). The procedure is detailed in Supplementary Materials S6.

In the initialization step, we fit independent GPs at each fidelity level and generate initial *pseudo* outputs $\{\tilde{\mathbf{y}}_l^{(0)}\}_{l=1}^{L-1}$ using their respective GP posterior mean. The initial parameter estimates are obtained using the *pseudo*-complete dataset $\{\{\mathbf{y}_l^{*(0)}\}_{l=1}^L, \{\mathcal{X}_l^*\}_{l=1}^L, \{t_l\}_{l=1}^L\}$.

In the E-step (imputation), we sample the pseudo outputs $\tilde{\mathbf{y}}_1^{(m)}$ from the posterior distribution $p(\tilde{\mathbf{y}}_1 | \mathbf{y}_1)$ and sample $\{\tilde{\mathbf{y}}_l^{(m)}\}_{l=2}^{L-1}$ from the conditional normal distribution $p(\{\tilde{\mathbf{y}}_l\}_{l=2}^{L-1} | Y_{-1})$, given fixed parameter estimates $\varphi^{(m-1)}$ and previous-step outputs $Y_{-L}^{*(m-1)} := \{\mathbf{y}_l^{*(m-1)}\}_{l=1}^{L-1}$. The imputed pseudo outputs are illustrated in Figure 7 for the non-additive example presented in Section 4 with non-nested input locations.

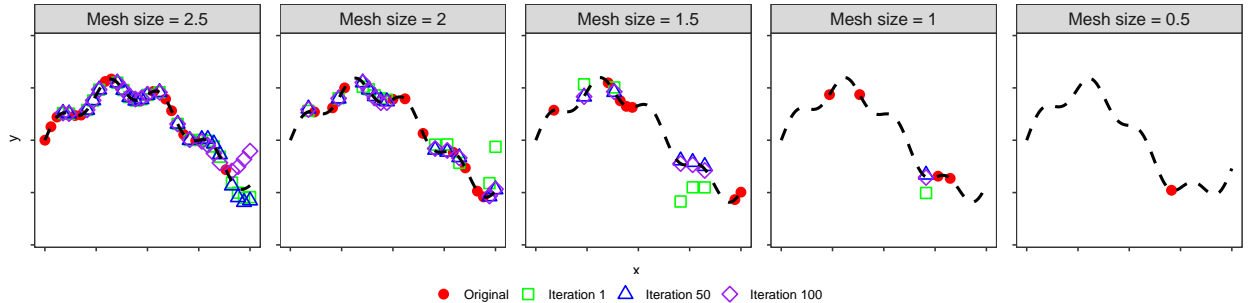


Figure 7: Illustration of pseudo-data generation for different tuning parameters. Each panel shows the true function (black dashed line), the original design points \mathcal{X}_l (red dots), and the pseudo-outputs $\tilde{\mathcal{X}}_l$ generated by the SEM method, with different shapes representing outputs from three SEM iterations.

With the pseudo-complete dataset $\{\{\mathbf{y}_l^{*(m)}\}_{l=1}^L, \{\mathcal{X}_l^*\}_{l=1}^L, \{t_l\}_{l=1}^L\}$, which follows a nested structure, we update the parameter estimates $\boldsymbol{\varphi}^{(m)}$ by maximizing the likelihood function as developed in Section 2.3. The iteration continues until reaching a prespecified number of iterations M , where we set $M = 100$ in the example presented later.

By alternating between a stochastic E-step and a deterministic M-step, the SEM algorithm constructs a Markov chain that does not converge to a single value but instead fluctuates around estimates that maximize the complete-data likelihood. To obtain a final estimate, we follow the approach of Ming et al. (2023), taking the average of the chain after discarding an initial burn-in period B :

$$\hat{\alpha} = \frac{1}{M - B} \sum_{m=B+1}^M \hat{\alpha}^{(m)}.$$

The same approach is used to estimate other parameters. Following Ming et al. (2023), we recommend setting $B = \lceil 0.75M \rceil$ (i.e., the smallest integer greater than or equal to $0.75M$).

6.2 Prediction

With the estimated parameters $\hat{\boldsymbol{\varphi}}$, we generate M pseudo-complete outputs, $\{Y^{*(m)}\}_{m=1}^M$, where each $Y^{*(m)} := \{\mathbf{y}_l^{*(m)}\}_{l=1}^L$, following the same procedure as in the E-step of the previous subsection. Using these generated samples, we compute the posterior mean and variance as follows:

$$\mu^{(m)}(t, \mathbf{x}) = \mathbb{E}[f(t, \mathbf{x})|Y^{*(m)}] \quad \text{and} \quad \sigma^{2(m)}(t, \mathbf{x}) = \mathbb{V}[f(t, \mathbf{x})|Y^{*(m)}]$$

for $l = 2, \dots, L$, and $\mu_l^{(m)}(\mathbf{x}) = \mathbb{E}[f_l(\mathbf{x})|Y^{*(m)}]$ and $\sigma_l^{2(m)}(\mathbf{x}) = \mathbb{V}[f_l(\mathbf{x})|Y^{*(m)}]$. These posterior means and variances follow the same closed-form expressions as h_1 and h_2 in Proposition 3.1, since the data has a nested structure with pseudo inputs and outputs. The only modification is the replacement of X_{-1} and Y_{-L} by X_{-1}^* and $Y_{-L}^{*(m)}$. The final predictive mean and variance

are then approximated as follows:

$$\mu^*(t, \mathbf{x}) \approx \frac{1}{M} \sum_{m=1}^M \mu^{(m)}(t, \mathbf{x}),$$

$$\sigma^{2*}(t, \mathbf{x}) \approx \frac{1}{M} \sum_{m=1}^M (\mu^{(m)}(t, \mathbf{x})^2 + \sigma^{2(m)}(t, \mathbf{x})) - \mu^*(t, \mathbf{x})^2.$$

Figure 8 illustrates the prediction results of the DNA model under a non-nested design for the non-additive example. Compared to the nested design (see Figure 3), the non-nested approach generally exhibits increased predictive uncertainty, which is expected due to the additional variability introduced by imputing pseudo-outputs rather than observing true outputs. Overall, the model still performs well: the posterior mean closely aligns with the truth function, and the confidence intervals successfully cover the true function.

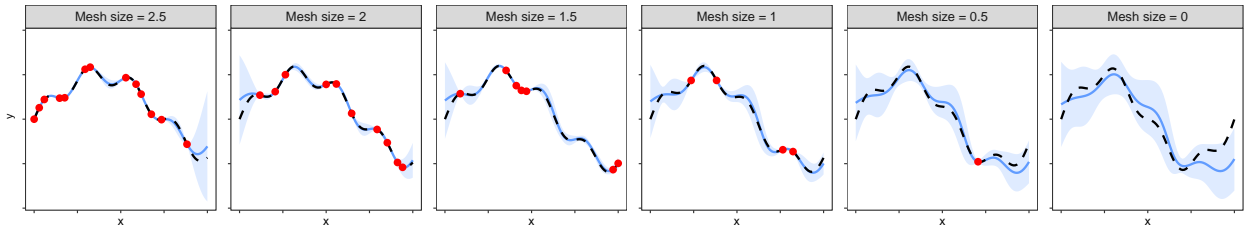


Figure 8: Illustration of the non-additive function in Section 4 under a non-nested design, along with predictions and 99% confidence intervals. In each subplot, the black dashed line represents the true function, red dots indicate design points, the blue line shows the predicted function, and the shaded region denotes the 99% confidence interval.

7 Conclusion and Discussion

We introduce the Diffusion Non-Additive (DNA) model for multi-fidelity simulations with tunable fidelity parameters, offering a flexible framework for modeling complex dependencies across fidelities. By relaxing the additive structure and allowing for a coupling between the fidelity-controlling parameter and the input space, the DNA model can adapt to a wide range of simulation behaviors. Through comprehensive numerical studies, including synthetic

functions and PDE-based simulators, we demonstrate that the DNA model achieves strong predictive performance and reliable uncertainty quantification. Future work will focus on establishing a rigorous theoretical foundation for the DNA model, including analyses of its asymptotic behavior when $t \rightarrow 0$.

The effectiveness of the DNA model motivates several promising avenues for future research. First, it has been noted that the Gneiting class can exhibit a *dimple property* (Kent et al., 2011), meaning that the covariance function is not monotonically decreasing with respect to temporal lag. To address this issue, Porcu et al. (2016) suggests using the great-circle distance instead of the Euclidean distance, while Cuevas et al. (2017) imposes a more restrictive condition on δ to ensure the absence of dimples. Further investigation into alternative constructions that avoid the dimple property while preserving flexibility and interpretability is worth exploring.

Another promising direction lies in extending the DNA model to accommodate high-dimensional outputs, which are common in finite element simulations that return spatial fields or outputs over many nodes. In such settings, direct emulation of each output dimension is often computationally infeasible and statistically inefficient. While various approaches have been proposed for high-dimensional outputs, such as principal component decomposition (Higdon et al., 2008), wavelet-based approach (Bayarri et al., 2007), P-splines (Williamson et al., 2012), and optimal basis selection (Salter et al., 2019), their extensions to the multi-fidelity framework remain scarce. Integrating these approaches within the DNA framework offers a valuable opportunity to achieve scalable emulation of high-dimensional outputs in a multi-fidelity setting.

Supplemental Materials Additional supporting materials can be found in Supplemental Materials, including the closed-form posterior mean and variance under an alternative kernel

based on the Matérn kernel, the proofs of Proposition 3.1 and Remark 2.1, and the detailed SEM algorithm in Section 6. The R code and package for reproducing the results in Sections 4 and 5 are also provided.

Data Availability Statement The authors confirm that the data supporting the findings of this study are available within its supplementary materials.

References

- Bayarri, M., Berger, J., Cafeo, J., Garcia-Donato, G., Liu, F., Palomo, J., Parthasarathy, R., Paulo, R., Sacks, J., and Walsh, D. (2007). Computer model validation with functional output. *The Annals of Statistics*, 35(5):1874–1906.
- Boutelet, R. and Sung, C.-L. (2025). Active learning for finite element simulations with adaptive non-stationary kernel function. *arXiv preprint arXiv:2503.23158*.
- Byrd, R. H., Lu, P., Nocedal, J., and Zhu, C. (1995). A limited memory algorithm for bound constrained optimization. *SIAM Journal on Scientific Computing*, 16(5):1190–1208.
- Celeux, G. and Diebolt, J. (1985). The SEM algorithm: a probabilistic teacher algorithm derived from the EM algorithm for the mixture problem. *Computational Statistics Quarterly*, 2(1):73–82.
- Clark, E., Brunton, S. L., and Kutz, J. N. (2020). Multi-fidelity sensor selection: Greedy algorithms to place cheap and expensive sensors with cost constraints. *IEEE Sensors Journal*, 21(1):600–611.
- Cressie, N. and Huang, H.-C. (1999). Classes of nonseparable, spatio-temporal stationary covariance functions. *Journal of the American Statistical Association*, 94(448):1330–1339.

- Cuevas, F., Porcu, E., and Bevilacqua, M. (2017). Contours and dimple for the Gneiting class of space-time correlation functions. *Biometrika*, 104(4):995–1001.
- Currin, C. (1988). A Bayesian approach to the design and analysis of computer experiments. Technical Report ORNL-6498, Oak Ridge National Lab. Oak Ridge, TN, USA.
- de la Hoz, F. and Vadillo, F. (2016). Numerical simulations of time-dependent partial differential equations. *Journal of Computational and Applied Mathematics*, 295:175–184.
- Dhatt, G., Lefrançois, E., and Touzot, G. (2012). *Finite Element Method*. John Wiley & Sons.
- Evans, L. C. (2010). *Partial Differential Equations*, volume 19. American Mathematical Society.
- Gneiting, T. (2002). Nonseparable, stationary covariance functions for space–time data. *Journal of the American Statistical Association*, 97(458):590–600.
- Gneiting, T. and Raftery, A. E. (2007). Strictly proper scoring rules, prediction, and estimation. *Journal of the American Statistical Association*, 102(477):359–378.
- Gramacy, R. B. (2020). *Surrogates: Gaussian Process Modeling, Design, and Optimization for the Applied Sciences*. CRC press.
- Haaland, B. and Qian, P. Z. G. (2010). An approach to constructing nested space-filling designs for multi-fidelity computer experiments. *Statistica Sinica*, 20(3):1063–1075.
- Hallmann, M., Schleich, B., and Wartzack, S. (2020). From tolerance allocation to tolerance-cost optimization: a comprehensive literature review. *The International Journal of Advanced Manufacturing Technology*, 107(11):4859–4912.

- He, X., Tuo, R., and Wu, C. F. J. (2017). Optimization of multi-fidelity computer experiments via the EQIE criterion. *Technometrics*, 59(1):58–68.
- Heo, J. and Sung, C.-L. (2025). Active learning for a recursive non-additive emulator for multi-fidelity computer experiments. *Technometrics*, 67(1):58–72.
- Higdon, D. (2002). Space and space-time modeling using process convolutions. In *Quantitative Methods for Current Environmental Issues*, pages 37–56. Springer.
- Higdon, D., Gattiker, J., Williams, B., and Rightley, M. (2008). Computer model calibration using high-dimensional output. *Journal of the American Statistical Association*, 103(482):570–583.
- Ho, J., Jain, A., and Abbeel, P. (2020). Denoising diffusion probabilistic models. *Advances in Neural Information Processing Systems*, 33:6840–6851.
- Ji, Y., Yuchi, H. S., Soeder, D., Paquet, J.-F., Bass, S. A., Joseph, V. R., Wu, C. J., and Mak, S. (2024). Conglomerate multi-fidelity gaussian process modeling, with application to heavy-ion collisions. *SIAM/ASA Journal on Uncertainty Quantification*, 12(2):473–502.
- Jin, Z., Li, B., Zhang, A., Cheng, J., Zhou, Q., and Xie, T. (2025). Multi-fidelity sequential optimisation method for metamaterials with negative Poisson’s ratio. *Journal of Engineering Design*, in press.
- Kennedy, M. C. and O’Hagan, A. (2000). Predicting the output from a complex computer code when fast approximations are available. *Biometrika*, 87(1):1–13.
- Kent, J. T., Mohammadzadeh, M., and Mosammam, A. M. (2011). The dimple in Gneiting’s spatial-temporal covariance model. *Biometrika*, 98(2):489–494.

- Kerleguer, B., Cannamela, C., and Garnier, J. (2024). A Bayesian neural network approach to multi-fidelity surrogate modelling. *International Journal for Uncertainty Quantification*, 14(1):43–60.
- Kyzyurova, K. N., Berger, J. O., and Wolpert, R. L. (2018). Coupling computer models through linking their statistical emulators. *SIAM/ASA Journal on Uncertainty Quantification*, 6(3):1151–1171.
- Le Gratiet, L. and Garnier, J. (2014). Recursive co-kriging model for design of computer experiments with multiple levels of fidelity. *International Journal for Uncertainty Quantification*, 4(5):365–386.
- Li, J., Vignal, P., Sun, S., and Calo, V. M. (2014). On stochastic error and computational efficiency of the Markov chain Monte Carlo method. *Communications in Computational Physics*, 16(2):467–490.
- Li, S., Xing, W., Kirby, R., and Zhe, S. (2020). Multi-fidelity Bayesian optimization via deep neural networks. *Advances in Neural Information Processing Systems*, 33:8521–8531.
- Mak, S., Sung, C.-L., Wang, X., Yeh, S.-T., Chang, Y.-H., Joseph, V. R., Yang, V., and Wu, C. F. J. (2018). An efficient surrogate model for emulation and physics extraction of large eddy simulations. *Journal of the American Statistical Association*, 113(524):1443–1456.
- MATLAB. (2021). *Version 9.11.0 (R2021b)*. Natick, Massachusetts: The MathWorks Inc.
- Ming, D. and Guillas, S. (2021). Linked Gaussian process emulation for systems of computer models using Matérn kernels and adaptive design. *SIAM/ASA Journal on Uncertainty Quantification*, 9(4):1615–1642.
- Ming, D., Williamson, D., and Guillas, S. (2023). Deep Gaussian process emulation using stochastic imputation. *Technometrics*, 65(2):150–161.

- Minka, T. P. (2001). Expectation propagation for approximate Bayesian inference. In *Proceedings of the Seventeenth Conference on Uncertainty in Artificial Intelligence*, pages 362–369.
- Oates, C. J., Karvonen, T., Teckentrup, A. L., Strocchi, M., and Niederer, S. A. (2025). Probabilistic richardson extrapolation. *Journal of the Royal Statistical Society Series B: Statistical Methodology*, 87(2):457–479.
- Oberkampf, W. L. and Roy, C. J. (2025). *Verification, Validation, and Uncertainty Quantification in Scientific Computing*. Cambridge University Press.
- Perdikaris, P., Raissi, M., Damianou, A., Lawrence, N. D., and Karniadakis, G. E. (2017). Non-linear information fusion algorithms for data-efficient multi-fidelity modelling. *Proceedings of the Royal Society A: Mathematical, Physical and Engineering Sciences*, 473(2198):20160751.
- Picheny, V., Ginsbourger, D., Richet, Y., and Caplin, G. (2013). Quantile-based optimization of noisy computer experiments with tunable precision. *Technometrics*, 55(1):2–13.
- Porcu, E., Bevilacqua, M., and Genton, M. G. (2016). Spatio-temporal covariance and cross-covariance functions of the great circle distance on a sphere. *Journal of the American Statistical Association*, 111(514):888–898.
- Porcu, E., Gregori, P., and Mateu, J. (2006). Nonseparable stationary anisotropic space–time covariance functions. *Stochastic Environmental Research and Risk Assessment*, 21(2):113–122.
- Qian, P. Z. G. (2009). Nested Latin hypercube designs. *Biometrika*, 96(4):957–970.
- Qian, P. Z. G., Ai, M., and Wu, C. F. J. (2009). Construction of nested space-filling designs. *The Annals of Statistics*, 37(6A):3616–3643.

- Qian, P. Z. G. and Wu, C. F. J. (2008). Bayesian hierarchical modeling for integrating low-accuracy and high-accuracy experiments. *Technometrics*, 50(2):192–204.
- Qian, Z., Seepersad, C. C., Joseph, V. R., Allen, J. K., and Wu, C. F. J. (2006). Building surrogate models based on detailed and approximate simulations. *Journal of Mechanical Design*, 128(4):668–677.
- Rasmussen, C. E. and Williams, C. K. (2006). *Gaussian Processes for Machine Learning*. Cambridge, MA: MIT Press.
- Rodrigues, A. and Diggle, P. J. (2010). A class of convolution-based models for spatio-temporal processes with non-separable covariance structure. *Scandinavian Journal of Statistics*, 37(4):553–567.
- Salter, J. M., Williamson, D. B., Scinocca, J., and Kharin, V. (2019). Uncertainty quantification for computer models with spatial output using calibration-optimal bases. *Journal of the American Statistical Association*, 114(528):1800–1814.
- Sendrea, R. E., Zekios, C. L., and Georgakopoulos, S. V. (2024). A review of multi-fidelity learning approaches for electromagnetic problems. *Electronics*, 14(1):89.
- Shi, X., Liu, Y., Xue, L., Chen, W., and Chyu, M. K. (2024). Prediction of supercritical CO₂ heat transfer behaviors by combining transfer learning and deep learning based on multi-fidelity data. *International Journal of Heat and Mass Transfer*, 218:124802.
- Song, D. and Joseph, V. R. (2025). Efficient active learning strategies for computer experiments. *arXiv preprint arXiv:2501.13841*.
- Stein, M. L. (1999). *Interpolation of Spatial Data: Some Theory for Kriging*. Springer Science & Business Media.

- Sung, C.-L., Ji, Y., Mak, S., Wang, W., and Tang, T. (2024). Stacking designs: Designing multifidelity computer experiments with target predictive accuracy. *SIAM/ASA Journal on Uncertainty Quantification*, 12(1):157–181.
- Tuo, R., Wu, C. F. J., and Yu, D. (2014). Surrogate modeling of computer experiments with different mesh densities. *Technometrics*, 56(3):372–380.
- Williamson, D., Goldstein, M., and Blaker, A. (2012). Fast linked analyses for scenario-based hierarchies. *Journal of the Royal Statistical Society Series C: Applied Statistics*, 61(5):665–691.
- Xiong, S., Qian, P. Z. G., and Wu, C. F. J. (2013). Sequential design and analysis of high-accuracy and low-accuracy computer codes. *Technometrics*, 55(1):37–46.
- Yang, Y., Deng, K., and Zhu, Y. (2026). Bayesian optimization with Pareto-principled training for economical hyperparameter optimization. *Statistica Sinica*, in press.
- Yuchi, H. S., Joseph, V. R., and Wu, C. F. J. (2023). Design and analysis of multifidelity finite element simulations. *Journal of Mechanical Design*, 145(6):061703.

Supplementary Materials for “Diffusion Non-Additive Emulator for Multi-Fidelity Simulations with Tunable Precision”

Junoh Heo, Romain Boutelet and Chih-Li Sung

Michigan State University

S1 Proof of Theorem 2.1

Let $\mathbf{K}_{\mathcal{X}} \in \mathbb{R}^{n \times n}$ denote the kernel matrix over \mathcal{X} with entries

$$[\mathbf{K}_{\mathcal{X}}]_{ij} = \exp \left(- \sum_{k=1}^d \frac{(x_{ik} - x_{jk})^2}{\theta_j} \right).$$

Suppose that the input locations in \mathcal{X} are distinct, then $\mathbf{K}_{\mathcal{X}}$ is strictly positive definite and thus full rank. The full kernel matrix across fidelity levels t_2, \dots, t_L can be expressed as

$$\mathbf{K}_{\delta} = \mathbf{G}_{\delta} \otimes \mathbf{K}_{\mathcal{X}},$$

where \otimes denotes the Kronecker product, and $\mathbf{G}_{\delta} \in \mathbb{R}^{L-1 \times L-1}$ has entries

$$[\mathbf{G}_{\delta}]_{ij} = \left(\frac{(t_i - t_j)^2}{\theta_t} + 1 \right)^{-\delta}, \quad \text{for } 2 \leq i, j \leq L.$$

When $\delta = 0$, each entry of \mathbf{G}_0 equals to 1, i.e., $\mathbf{G}_0 = \mathbf{1}_{L-1} \mathbf{1}_{L-1}^{\top}$, which is a rank-one positive semi-definite matrix. Consequently,

$$\mathbf{K}_0 = \mathbf{G}_0 \otimes \mathbf{K}_{\mathcal{X}} = (\mathbf{1}_{L-1} \mathbf{1}_{L-1}^{\top}) \otimes \mathbf{K}_{\mathcal{X}},$$

is positive semi-definite but has rank only $1 \times n = n$, despite being of size $n(L-1) \times n(L-1)$. Since $\mathbf{K}_{\mathcal{X}} \succ 0$ and $\mathbf{G}_0 \succeq 0$, we conclude that \mathbf{K}_0 is positive semi-definite but singular, with $\lambda_{\min}(\mathbf{K}_0) = 0$, and condition number $\kappa(\mathbf{K}_0) = \infty$.

When $\delta > 0$, the function $f_\delta(r) = (r+1)^{-\delta}$ is completely monotonic on $[0, \infty)$. By Schoenberg's theorem (Schoenberg, 1938), the matrix \mathbf{G}_δ with entries $f_\delta((t_i - t_j)^2 / \theta_t)$ is strictly positive definite, since the tuning parameters t_2, \dots, t_L are distinct. Given that $\mathbf{K}_{\mathcal{X}} \succ 0$, the Kronecker product $\mathbf{K}_\delta = \mathbf{G}_\delta \otimes \mathbf{K}_{\mathcal{X}}$ is also strictly positive definite. Consequently, $\lambda_{\min}(\mathbf{K}_\delta) > 0$. Moreover, since \mathbf{K}_δ is symmetric and finite-dimensional with size $n(L-1) \times n(L-1)$, all its eigenvalues are real and bounded, implying $\lambda_{\max}(\mathbf{K}_\delta) < \infty$. It follows that $\kappa(\mathbf{K}_\delta) < \infty$.

Thus, for any $\delta > 0$, we conclude that $\kappa(\mathbf{K}_\delta) < \kappa(\mathbf{K}_0)$.

S2 The gradient of the log-likelihood

The gradient of the log-likelihood function (9) with respect to any parameter $\eta \in (\{\theta_j\}_{j=1}^d, \theta_y, \theta_t, \beta, \delta)$ is given by

$$-\frac{1}{2} \frac{\partial \log(\det(\mathbf{K}))}{\partial \eta} + \frac{N_{-1}}{2} \frac{(Y_{-1} - \hat{\alpha} \mathbf{1}_{N_{-1}})^T \mathbf{K}^{-1} \frac{\partial \mathbf{K}^{-1}}{\partial \eta} \mathbf{K}^{-1} (Y_{-1} - \hat{\alpha} \mathbf{1}_{N_{-1}})}{(Y_{-1} - \hat{\alpha} \mathbf{1}_{N_{-1}})^T \mathbf{K}^{-1} (Y_{-1} - \hat{\alpha} \mathbf{1}_{N_{-1}})}.$$

To compute the partial derivatives, we use

$$\frac{\partial \mathbf{K}^{-1}}{\partial \eta} = -\mathbf{K}^{-1} \frac{\partial \mathbf{K}}{\partial \eta} \mathbf{K}^{-1}, \quad \frac{\partial \log(\det(\mathbf{K}))}{\partial \eta} = \text{tr} \left(\mathbf{K}^{-1} \frac{\partial \mathbf{K}}{\partial \eta} \right).$$

Hence, it remains to compute $\frac{\partial \mathbf{K}}{\partial \eta}$. For the nonseparable squared exponential kernel in (6), we have the following expressions:

$$\begin{aligned}\frac{\partial \mathbf{K}}{\partial \theta_j} &= -\frac{\|x_j - x'_j\|^2}{\theta_j^2} \frac{\partial \mathbf{K}}{\partial v}, & \frac{\partial \mathbf{K}}{\partial \theta_y} &= -\frac{\|y - y'\|^2}{\theta_y^2} \frac{\partial \mathbf{K}}{\partial v}, \\ \frac{\partial \mathbf{K}}{\partial \theta_t} &= \frac{(t - t')^2}{\theta_t^2} u^2 \frac{\partial \mathbf{K}}{\partial u}, \\ \frac{\partial \mathbf{K}}{\partial \beta} &= \mathbf{K} \log u \left(\frac{d+1}{2} - u^\beta v \right), \\ \frac{\partial \mathbf{K}}{\partial \delta} &= \mathbf{K} \log u,\end{aligned}$$

where $u = \left(1 + \frac{(t-t')^2}{\theta_t^2}\right)^{-1}$, $v = \frac{\|y-y'\|^2}{\theta_y^2} + \sum_{j=1}^d \frac{\|x_j-x'_j\|^2}{\theta_j^2}$, and

$$\begin{aligned}\frac{\partial \mathbf{K}}{\partial u} &= \left(\frac{d+1}{2} \beta + \delta - \beta u^\beta v \right) u^{\frac{d+1}{2} \beta + \delta - 1} \exp(-u^\beta v), \\ \frac{\partial \mathbf{K}}{\partial v} &= -u^{\frac{d+3}{2} \beta + \delta} \exp(-u^\beta v).\end{aligned}$$

For the nonseparable Matérn kernel (introduced in Section S4) with $\nu = 1.5$, we have

$$\begin{aligned}\frac{\partial \mathbf{K}}{\partial \theta_j} &= -\frac{v_j}{\theta_j} \frac{\partial \mathbf{K}}{\partial v_j}, & \frac{\partial \mathbf{K}}{\partial \theta_y} &= -\frac{v_y}{\theta_y} \frac{\partial \mathbf{K}}{\partial v_y} \\ \frac{\partial \mathbf{K}}{\partial \theta_t} &= \frac{(t - t')^2}{\theta_t^2} u^2 \frac{\partial \mathbf{K}}{\partial u}, \\ \frac{\partial \mathbf{K}}{\partial \beta} &= \mathbf{K} \frac{\log u}{2} \left((d+1) - \left(\sum_{j=1}^d \frac{(u^{\frac{\beta}{2}} v_j)^2}{1 + u^{\frac{\beta}{2}} v_j} + \frac{(u^{\frac{\beta}{2}} v_y)^2}{1 + u^{\frac{\beta}{2}} v_y} \right) \right), \\ \frac{\partial \mathbf{K}}{\partial \delta} &= \mathbf{K} \log u,\end{aligned}$$

where $u = \left(1 + \frac{(t-t')^2}{\theta_t}\right)^{-1}$, $v_j = \frac{\sqrt{3}\|x_j - x'_j\|}{\theta_j}$, $v_y = \frac{\sqrt{3}\|y - y'\|}{\theta_y}$, and

$$\begin{aligned}\frac{\partial \mathbf{K}}{\partial u} &= \mathbf{K} \left(\frac{\frac{(d+1)\beta + \delta}{2}}{u} - \frac{\beta}{2} u^{-1} \left(\sum_{j=1}^d \frac{(u^{\frac{\beta}{2}} v_j)^2}{1 + u^{\frac{\beta}{2}} v_j} + \frac{(u^{\frac{\beta}{2}} v_y)^2}{1 + u^{\frac{\beta}{2}} v_y} \right) \right), \\ \frac{\partial \mathbf{K}}{\partial v_j} &= -\mathbf{K} \frac{u^{\frac{\beta}{2}} v_j}{1 + u^{\frac{\beta}{2}} v_j}, \quad \frac{\partial \mathbf{K}}{\partial v_y} = -\mathbf{K} \frac{u^{\frac{\beta}{2}} v_y}{1 + u^{\frac{\beta}{2}} v_y}.\end{aligned}$$

For the nonseparable Matérn kernel with $\nu = 2.5$, we have

$$\begin{aligned}\frac{\partial \mathbf{K}}{\partial \theta_j} &= -\frac{v_j}{\theta_j} \frac{\partial \mathbf{K}}{\partial v_j}, \quad \frac{\partial \mathbf{K}}{\partial \theta_y} = -\frac{v_y}{\theta_y} \frac{\partial \mathbf{K}}{\partial v_y}, \\ \frac{\partial \mathbf{K}}{\partial \theta_t} &= \frac{(t-t')^2}{\theta_t^2} u^2 \frac{\partial \mathbf{K}}{\partial u}, \\ \frac{\partial \mathbf{K}}{\partial \beta} &= \mathbf{K} \frac{\log u}{2} \left((d+1) - \left(\sum_{j=1}^d \frac{(u^{\frac{\beta}{2}} v_j)^2 (1 + u^{\frac{\beta}{2}} v_j)}{3(1 + u^{\frac{\beta}{2}} v_j + \frac{(u^{\frac{\beta}{2}} v_j)^2}{3})} + \frac{(u^{\frac{\beta}{2}} v_y)^2 (1 + u^{\frac{\beta}{2}} v_y)}{3(1 + u^{\frac{\beta}{2}} v_y + \frac{(u^{\frac{\beta}{2}} v_y)^2}{3})} \right) \right), \\ \frac{\partial \mathbf{K}}{\partial \delta} &= \mathbf{K} \log u,\end{aligned}$$

where $u = \left(1 + \frac{(t-t')^2}{\theta_t}\right)^{-1}$, $v_j = \frac{\sqrt{5}\|x_j - x'_j\|}{\theta_j}$, $v_y = \frac{\sqrt{5}\|y - y'\|}{\theta_y}$, and

$$\begin{aligned}\frac{\partial \mathbf{K}}{\partial u} &= \mathbf{K} \left(\frac{\frac{(d+1)\beta + \delta}{2}}{u} - \frac{\beta}{2} u^{-1} \left(\sum_{j=1}^d \frac{(u^{\frac{\beta}{2}} v_j)^2 (1 + u^{\frac{\beta}{2}} v_j)}{3(1 + u^{\frac{\beta}{2}} v_j + \frac{(u^{\frac{\beta}{2}} v_j)^2}{3})} + \frac{(u^{\frac{\beta}{2}} v_y)^2 (1 + u^{\frac{\beta}{2}} v_y)}{3(1 + u^{\frac{\beta}{2}} v_y + \frac{(u^{\frac{\beta}{2}} v_y)^2}{3})} \right) \right), \\ \frac{\partial \mathbf{K}}{\partial v_j} &= -\mathbf{K} \frac{u^{\frac{\beta}{2}} v_j (1 + u^{\frac{\beta}{2}} v_j)}{3(1 + u^{\frac{\beta}{2}} v_j + \frac{(u^{\frac{\beta}{2}} v_j)^2}{3})} u^{\frac{\beta}{2}}, \quad \frac{\partial \mathbf{K}}{\partial v_y} = -\mathbf{K} \frac{u^{\frac{\beta}{2}} v_y (1 + u^{\frac{\beta}{2}} v_y)}{3(1 + u^{\frac{\beta}{2}} v_y + \frac{(u^{\frac{\beta}{2}} v_y)^2}{3})} u^{\frac{\beta}{2}}.\end{aligned}$$

S3 Posterior mean and variance of DNA model

The posterior mean and variance at the input \mathbf{x} can be derived as follows,

$$\begin{aligned}
\mu_l^*(\mathbf{x}) &= \mathbb{E}[f_l(\mathbf{x})|Y_N] = \alpha + \mathbb{E}[\mathbf{k}(t, \mathbf{x}, f_{l-1}(\mathbf{x}))^T | Y_N] \mathbf{K}^{-1} (Y_{-1} - \alpha \mathbf{1}_{N-1}) \\
&= \alpha + \sum_{i=1}^{N-1} r_i c_i^{\frac{d+1}{2} + \frac{\delta}{\beta}} \prod_{j=1}^d \exp\left(-c_i \frac{(x_j - (\mathbf{X}_{-1})_{ij})^2}{\theta_j}\right) \mathbb{E}\left[\exp\left\{-c_i \frac{((Y_{-L})_i - f_{l-1}(\mathbf{x}))^2}{\theta_y}\right\} \middle| Y_N\right] \\
&= \alpha + \sum_{i=1}^{N-1} r_i c_i^{\frac{d+1}{2} + \frac{\delta}{\beta}} \prod_{j=1}^d \exp\left(-c_i \frac{(x_j - (\mathbf{X}_{-1})_{ij})^2}{\theta_j}\right) \sqrt{\frac{\theta_y}{\theta_y + 2\sigma_{l-1}^{*2}(\mathbf{x})}} \exp\left(-c_i \frac{((Y_{-L})_i - \mu_{l-1}^*(\mathbf{x}))^2}{\theta_y + 2\sigma_{l-1}^{*2}(\mathbf{x})}\right) \\
&= \alpha + \sqrt{\frac{\theta_y}{\theta_y + 2\sigma_{l-1}^{*2}(\mathbf{x})}} \sum_{i=1}^{N-1} r_i c_i^{\frac{d+1}{2} + \frac{\delta}{\beta}} \exp\left(-c_i \left\{ \sum_{j=1}^d \frac{(x_j - (\mathbf{X}_{-1})_{ij})^2}{\theta_j} + \frac{((Y_{-L})_i - \mu_{l-1}^*(\mathbf{x}))^2}{\theta_y + 2\sigma_{l-1}^{*2}(\mathbf{x})} \right\}\right),
\end{aligned}$$

and

$$\begin{aligned}
\sigma_l^{*2}(\mathbf{x}) &= \mathbb{V}[f_l(\mathbf{x})|Y_N] = \mathbb{V}[\mathbb{E}[f_l(\mathbf{x})|f_{l-1}(\mathbf{x}), Y_N]] + \mathbb{E}[\mathbb{V}[f_l(\mathbf{x})|f_{l-1}(\mathbf{x}), Y_N]] \\
&= \mathbb{E}\left[\{\mathbb{E}[f_l(\mathbf{x})|f_{l-1}(\mathbf{x}), Y_N]\}^2\right] - \mu_l^*(\mathbf{x})^2 + \mathbb{E}[\mathbb{V}[f_l(\mathbf{x})|f_{l-1}(\mathbf{x}), Y_N]] \\
&= \mathbb{E}\left[\left\{\alpha + \mathbf{k}(t_l, \mathbf{x}, f_{l-1}(\mathbf{x}))^T \mathbf{K}^{-1} (Y_{-1} - \alpha \mathbf{1}_{N-1})\right\}^2 \middle| Y_N\right] - \mu_l^*(\mathbf{x})^2 \\
&\quad + \mathbb{E}\left[\tau^2 \left\{1 - \mathbf{k}(t_l, \mathbf{x}, f_{l-1}(\mathbf{x}))^T \mathbf{K}^{-1} \mathbf{k}(t_l, \mathbf{x}, f_{l-1}(\mathbf{x}))\right\} \middle| Y_N\right] \\
&= \alpha^2 + 2\alpha(\mu_l^*(\mathbf{x}) - \alpha) + \mathbb{E}\left[\left\{\mathbf{k}(t_l, \mathbf{x}, f_{l-1}(\mathbf{x}))^T \mathbf{K}^{-1} (Y_{-1} - \alpha \mathbf{1}_{N-1})\right\}^2 \middle| Y_N\right] \\
&\quad - \mu_l^*(\mathbf{x})^2 + \tau^2 - \tau^2 \mathbb{E}\left[\left\{\mathbf{k}(t_l, \mathbf{x}, f_{l-1}(\mathbf{x}))^T \mathbf{K}^{-1} \mathbf{k}(t_l, \mathbf{x}, f_{l-1}(\mathbf{x}))\right\} \middle| Y_N\right] \\
&= \tau^2 - (\mu_l^*(\mathbf{x}) - \alpha)^2 + \\
&\quad + \mathbb{E}\left[\mathbf{k}(t_l, \mathbf{x}, f_{l-1}(\mathbf{x}))^T \left\{\mathbf{K}^{-1} (Y_{-1} - \alpha \mathbf{1}_{N-1}) (Y_{-1} - \alpha \mathbf{1}_{N-1})^T \mathbf{K}^{-1} - \tau^2 \mathbf{K}^{-1}\right\} \mathbf{k}(t_l, \mathbf{x}, f_{l-1}(\mathbf{x})) \middle| Y_N\right] \\
&= \tau^2 - (\mu_l^*(\mathbf{x}) - \alpha)^2 + \left(\sum_{i,k=1}^{N-1} (r_i r_k - \tau^2 (\mathbf{K}^{-1})_{ik}) (c_i c_k)^{\frac{d+1}{2} + \frac{\delta}{\beta}}\right)
\end{aligned}$$

$$\begin{aligned}
& \times \exp \left(- \sum_{j=1}^d \frac{c_i(x_j - (\mathbf{X}_{-1})_{ij})^2 + c_k(x_j - (\mathbf{X}_{-1})_{kj})^2}{\theta_j} \right) \\
& \times \mathbb{E} \left[\exp \left(- \frac{c_i(f_{l-1}(\mathbf{x}) - (Y_{-L})_i)^2 + c_k(f_{l-1}(\mathbf{x}) - (Y_{-L})_k)^2}{\theta_y} \right) \middle| Y_N \right] \quad (\text{S3.1}) \\
& = \tau^2 - (\mu_l^*(\mathbf{x}) - \alpha)^2 + \left(\sum_{i,k=1}^{N-1} \zeta_{ik}(\mu_{l-1}^*(\mathbf{x}), \sigma_{l-1}^{*2}(\mathbf{x})) (r_i r_k - \tau^2 (\mathbf{K}^{-1})_{ik}) (c_i c_k)^{\frac{d+1}{2} + \frac{\delta}{\beta}} \right. \\
& \quad \left. \times \exp \left(- \sum_{j=1}^d \frac{c_i(x_j - (\mathbf{X}_{-1})_{ij})^2 + c_k(x_j - (\mathbf{X}_{-1})_{kj})^2}{\theta_j} \right) \right),
\end{aligned}$$

where $r_i = (\mathbf{K}^{-1}(Y_{-1} - \alpha \mathbf{1}_{N-1}))_i$, $c_i = c(t, \mathbf{t}_i) = \left(\frac{(t - \mathbf{t}_i)^2}{\theta_t} + 1 \right)^{-\beta}$ and

$$\begin{aligned}
\zeta_{ik}(\mu, \sigma^2) &= \sqrt{\frac{\theta_y}{\theta_y + 2(c_i + c_k)\sigma^2}} \\
& \times \exp \left(- \frac{c_i((Y_{-L})_i - \mu)^2 + c_k((Y_{-L})_k - \mu)^2 + \frac{2}{\theta_y} c_i c_k \sigma^2 ((Y_{-L})_i - (Y_{-L})_k)^2}{\theta_y + 2(c_i + c_k)\sigma^2} \right).
\end{aligned}$$

For a random variable $X \sim N(\mu, \sigma^2)$, we obtain the expression in (S3.1) as follows:

$$\begin{aligned}
\frac{1}{\sqrt{2\pi\sigma^2}} \int \exp(-Ax^2 + Bx - C) dx &= \frac{1}{\sqrt{2\pi\sigma^2}} \int \exp \left(-A \left(x - \frac{B}{2A} \right)^2 + \frac{B^2}{4A} - C \right) dx \\
&= \frac{1}{\sqrt{2\pi\sigma^2}} \exp \left(\frac{B^2}{4A} - C \right) \int \exp \left(-A \left(x - \frac{B}{2A} \right)^2 \right) dx \\
&= \frac{1}{\sqrt{2\pi\sigma^2}} \exp \left(\frac{B^2}{4A} - C \right) \sqrt{\frac{\pi}{A}} \\
&= \frac{1}{\sqrt{2\sigma^2 A}} \exp \left(\frac{B^2}{4A} - C \right).
\end{aligned}$$

Thus,

$$\begin{aligned}
\mathbb{E} \left[\exp \left(-c_1(X - y_i)^2 - c_2(X - y_k)^2 \right) \middle| Y_N \right] &= \int \frac{1}{\sqrt{2\pi\sigma^2}} e^{(-c_1(x-y_i)^2 - c_2(x-y_k)^2)} e^{\left(-\frac{(x-\mu)^2}{2\sigma^2}\right)} dx \\
&= \frac{1}{\sqrt{2\pi\sigma^2}} \int \exp \left(- \left(c_1 + c_2 + \frac{1}{2\sigma^2} \right) x^2 + \left(2c_1y_i + 2c_2y_k + \frac{2\mu}{2\sigma^2} \right) x - \left(c_1y_i^2 + c_2y_k^2 + \frac{\mu^2}{2\sigma^2} \right) \right) dx \\
&= \frac{1}{\sqrt{2\sigma^2 \left(c_1 + c_2 + \frac{1}{2\sigma^2} \right)}} \exp \left(\frac{\left(2c_1y_i + 2c_2y_k + \frac{2\mu}{2\sigma^2} \right)^2}{4 \left(c_1 + c_2 + \frac{1}{2\sigma^2} \right)} - \left(c_1y_i^2 + c_2y_k^2 + \frac{\mu^2}{2\sigma^2} \right) \right) \\
&= \frac{1}{\sqrt{1 + 2 \left(c_1 + c_2 \right) \sigma^2}} \exp \left(\frac{\left(2 \left(c_1y_i + c_2y_k \right) \sigma^2 + \mu \right)^2}{2\sigma^2 \left(1 + 2 \left(c_1 + c_2 \right) \sigma^2 \right)} - \frac{2 \left(c_1y_i^2 + c_2y_k^2 \right) \sigma^2 + \mu^2}{2\sigma^2} \right) \\
&= \frac{1}{\sqrt{1 + 2 \left(c_1 + c_2 \right) \sigma^2}} \exp \left(- \frac{c_1 \left(y_i - \mu \right)^2 + c_2 \left(y_k - \mu \right)^2 + 2c_1c_2\sigma^2 \left(y_i - y_k \right)^2}{\left(1 + 2 \left(c_1 + c_2 \right) \sigma^2 \right)} \right),
\end{aligned}$$

where $\mu = \mu_{l-1}^*(\mathbf{x})$, $\sigma^2 = \sigma_{l-1}^{*2}(\mathbf{x})$, $c_1 = \frac{c_i}{\theta_y}$, $c_2 = \frac{c_k}{\theta_y}$, $y_i = (Y_{-L})_i$, and $y_k = (Y_{-L})_k$. Therefore,

$$\begin{aligned}
\zeta_{ik}(\mu, \sigma^2) &= \sqrt{\frac{\theta_y}{\theta_y + 2(c_i + c_k)\sigma^2}} \\
&\quad \times \exp \left(- \frac{c_i \left((Y_{-L})_i - \mu \right)^2 + c_k \left((Y_{-L})_k - \mu \right)^2 + \frac{2}{\theta_y} c_i c_k \sigma^2 \left((Y_{-L})_i - (Y_{-L})_k \right)^2}{\theta_y + 2(c_i + c_k)\sigma^2} \right).
\end{aligned}$$

S4 Nonseparable Matérn kernel functions

The section introduces the nonseparable Matérn kernels with smoothness parameters of

$\nu = 1.5$ and $\nu = 2.5$. Denote

$$\psi(x, x'; \theta, \nu = 1.5) = \left(1 + \frac{1}{\left(\frac{(t-t')^2}{\theta_t} + 1 \right)^{\frac{\beta}{2}}} \frac{\sqrt{3}|x - x'|}{\theta} \right) \exp \left(- \frac{1}{\left(\frac{(t-t')^2}{\theta_t} + 1 \right)^{\frac{\beta}{2}}} \frac{\sqrt{3}|x - x'|}{\theta} \right),$$

$$\begin{aligned} \psi(x, x'; \theta, \nu = 2.5) &= \left(1 + \frac{1}{\left(\frac{(t-t')^2}{\theta_t} + 1\right)^{\frac{\beta}{2}}} \frac{\sqrt{5}|x-x'|}{\theta} + \frac{1}{3} \left(\frac{1}{\left(\frac{(t-t')^2}{\theta_t} + 1\right)^{\frac{\beta}{2}}} \frac{\sqrt{5}|x-x'|}{\theta} \right)^2 \right) \\ &\quad \times \exp \left(-\frac{1}{\left(\frac{(t-t')^2}{\theta_t} + 1\right)^{\frac{\beta}{2}}} \frac{\sqrt{5}|x-x'|}{\theta} \right). \end{aligned}$$

The nonseparable Matérn kernel function is denoted by

$$K((t, \mathbf{x}, y), (t', \mathbf{x}', y'); \nu) = \left(\frac{(t-t')^2}{\theta_t} + 1 \right)^{-\left(\frac{\beta(d+1)}{2} + \delta\right)} \psi(y, y'; \theta_y, \nu) \prod_{j=1}^d \psi(x_j, x'_j; \theta_j, \nu).$$

S5 Posterior mean and variance under Matérn kernel

This section is developed along the line of Ming and Guillas (2021). The posterior mean and variance at the input \mathbf{x} can be derived as follows,

$$\begin{aligned} \mu_l^*(\mathbf{x}) &= \mathbb{E}[f_l(\mathbf{x})|Y_N] \\ &= \alpha + \mathbb{E}[\mathbf{k}(t_l, \mathbf{x}, f_{l-1}(\mathbf{x}))^T | Y_N] \mathbf{K}^{-1} (Y_{-1} - \alpha \mathbf{1}_{N-1}) \\ &= \alpha + \sum_{i=1}^{N-1} r_i c_i(t_l)^{(d+1) + \frac{2\delta}{\beta}} \xi_i \prod_{j=1}^d \psi(x_j, (\mathbf{X}_{-1})_{ij}; \theta_{lj}, \nu), \\ \sigma_l^{*2}(\mathbf{x}) &= \mathbb{V}[f_l(\mathbf{x})|Y_N] \\ &= \alpha^2 + 2\alpha(\mu_l^*(\mathbf{x}) - \alpha) + \mathbb{E} \left[\left\{ \mathbf{k}(t_l, \mathbf{x}, f_{l-1}(\mathbf{x}))^T \mathbf{K}^{-1} (Y_{-1} - \alpha \mathbf{1}_{N-1}) \right\}^2 | Y_N \right] \\ &\quad - \mu_l^{*2}(\mathbf{x}) + \tau^2 - \tau^2 \mathbb{E} \left[\left\{ \mathbf{k}(t_l, \mathbf{x}, f_{l-1}(\mathbf{x}))^T \mathbf{K}^{-1} \mathbf{k}(t_l, \mathbf{x}, f_{l-1}(\mathbf{x})) \right\} | Y_N \right] \\ &= \tau^2 - (\mu_l^*(\mathbf{x}) - \alpha)^2 \\ &+ \left(\sum_{i,k=1}^{N-1} \zeta_{ik} (r_i r_k - \tau^2 (\mathbf{K}^{-1})_{ik}) (c_i(t_l) c_k(t_l))^{(d+1) + \frac{2\delta}{\beta}} \prod_{j=1}^d \psi(x_j, (\mathbf{X}_{-1})_{ij}; \theta_j, \nu) \psi(x_j, (\mathbf{X}_{-1})_{kj}; \theta_j, \nu) \right) \end{aligned}$$

where ψ is defined in Section S4, $r_i = (\mathbf{K}^{-1}(Y_{-L} - \alpha \mathbf{1}_{N_{-L}}))_i$, $c_i(t) := c(t, \mathbf{t}_i) = \left(\frac{(t - \mathbf{t}_i)^2}{\theta_t} + 1\right)^{-\frac{\beta}{2}}$, $\xi_i = \mathbb{E} \left[\psi(f_{l-1}(\mathbf{x}), (Y_{-L})_i; \theta_y, \nu) \middle| Y_N \right]$, and $\zeta_{ik} = \mathbb{E} \left[\psi(f_{l-1}(\mathbf{x}), (Y_{-L})_i; \theta_y, \nu) \psi(f_{l-1}(\mathbf{x}), (Y_{-L})_k; \theta_y, \nu) \middle| Y_N \right]$. The closed-form expressions of ξ_i and ζ_{ik} are provided in the following subsections.

S5.1 Matérn-1.5 kernel

For Matérn kernel with the smoothness parameter of 1.5, ξ_i and ζ_{ik} are provided as follows,

$$\begin{aligned} \xi_i &= \exp \left(\frac{3c_i^2(t)\sigma_{l-1}^{*2}(\mathbf{x}) + 2\sqrt{3}c_i(t)\theta_y((Y_{-L})_i - \mu_{l-1}^*(\mathbf{x}))}{2\theta_y^2} \right) \\ &\times \left[E'_1 \Lambda_{11} \Phi \left(\frac{\mu_{l-1}^*(\mathbf{x}) - (Y_{-L})_i - \frac{\sqrt{3}c_i(t)\sigma_{l-1}^{*2}(\mathbf{x})}{\theta_y}}{\sigma_{l-1}^*(\mathbf{x})} \right) \right. \\ &+ E'_1 \Lambda_{12} \frac{\sigma_{l-1}^*(\mathbf{x})}{\sqrt{2\pi}} \exp \left(-\frac{\left((Y_{-L})_i - \mu_{l-1}^*(\mathbf{x}) + \frac{\sqrt{3}c_i(t)\sigma_{l-1}^{*2}(\mathbf{x})}{\theta_y} \right)^2}{2\sigma_{l-1}^{*2}(\mathbf{x})} \right) \left. \right] \\ &+ \exp \left(\frac{3c_i^2(t)\sigma_{l-1}^{*2}(\mathbf{x}) - 2\sqrt{3}c_i(t)\theta_y((Y_{-L})_i - \mu_{l-1}^*(\mathbf{x}))}{2\theta_y^2} \right) \\ &\times \left[E'_2 \Lambda_{21} \Phi \left(\frac{-\mu_{l-1}^*(\mathbf{x}) + (Y_{-L})_i - \frac{\sqrt{3}c_i(t)\sigma_{l-1}^{*2}(\mathbf{x})}{\theta_y}}{\sigma_{l-1}^*(\mathbf{x})} \right) \right. \\ &+ E'_2 \Lambda_{12} \cdot \frac{\sigma_{l-1}^*(\mathbf{x})}{\sqrt{2\pi}} \exp \left(-\frac{\left((Y_{-L})_i - \mu_{l-1}^*(\mathbf{x}) - \frac{\sqrt{3}c_i(t)\sigma_{l-1}^{*2}(\mathbf{x})}{\theta_y} \right)^2}{2\sigma_{l-1}^{*2}(\mathbf{x})} \right) \left. \right], \end{aligned}$$

$$\begin{aligned}
\zeta_{ik} = & \exp \left\{ \frac{3\sigma_{l-1}^{*2}(\mathbf{x})(c_i(t) + c_k(t))^2 + 2\sqrt{3}\theta_y (c_i(t)((Y_{-L})_i - \mu_{l-1}^*(\mathbf{x})) + c_k(t)((Y_{-L})_k - \mu_{l-1}^*(\mathbf{x})))}{2\theta_y^2} \right\} \\
& \times \left[E'_3 \Lambda_{31} \Phi \left\{ \frac{\left(\mu_{l-1}^*(\mathbf{x}) - (Y_{-L})_k - \sqrt{3}(c_i(t) + c_k(t)) \frac{\sigma_{l-1}^{*2}(\mathbf{x})}{\theta_y} \right)}{\sigma_{l-1}^*(\mathbf{x})} \right\} \right. \\
& + E'_3 \Lambda_{32} \frac{\sigma_{l-1}^*(\mathbf{x})}{\sqrt{2\pi}} \exp \left(- \frac{\left((Y_{-L})_k - \mu_{l-1}^*(\mathbf{x}) + \sqrt{3}(c_i(t) + c_k(t)) \frac{\sigma_{l-1}^{*2}(\mathbf{x})}{\theta_y} \right)^2}{2\sigma_{l-1}^{*2}(\mathbf{x})} \right) \left. \right] \\
& + \exp \left\{ \frac{3\sigma_{l-1}^{*2}(\mathbf{x})(c_i(t) - c_k(t))^2 + 2\sqrt{3}\theta_y (c_i(t)((Y_{-L})_i - \mu_{l-1}^*(\mathbf{x})) - c_k(t)((Y_{-L})_k - \mu_{l-1}^*(\mathbf{x})))}{2\theta_y^2} \right\} \\
& \times \left[E'_4 \Lambda_{41} \left(\Phi \left\{ \frac{(Y_{-L})_k - \mu_{l-1}^*(\mathbf{x})}{\sigma_{l-1}^*(\mathbf{x})} \right\} - \Phi \left\{ \frac{(Y_{-L})_i - \mu_{l-1}^*(\mathbf{x})}{\sigma_{l-1}^*(\mathbf{x})} \right\} \right) \right. \\
& + E'_4 \Lambda_{42} \frac{\sigma_{l-1}^*(\mathbf{x})}{\sqrt{2\pi}} \exp \left(- \frac{\left((Y_{-L})_i - \mu_{l-1}^*(\mathbf{x}) \right)^2}{2\sigma_{l-1}^{*2}(\mathbf{x})} \right) - E'_4 \Lambda_{43} \frac{\sigma_{l-1}^*(\mathbf{x})}{\sqrt{2\pi}} \exp \left(- \frac{\left((Y_{-L})_k - \mu_{l-1}^*(\mathbf{x}) \right)^2}{2\sigma_{l-1}^{*2}(\mathbf{x})} \right) \left. \right] \\
& + \exp \left\{ \frac{3\sigma_{l-1}^{*2}(\mathbf{x})(c_i(t) + c_k(t))^2 - 2\sqrt{3}\theta_y (c_i(t)((Y_{-L})_i - \mu_{l-1}^*(\mathbf{x})) + c_k(t)((Y_{-L})_k - \mu_{l-1}^*(\mathbf{x})))}{2\theta_y^2} \right\} \\
& \times \left[E'_5 \Lambda_{51} \Phi \left\{ \frac{\left(-\mu_{l-1}^*(\mathbf{x}) + (Y_{-L})_i - \sqrt{3}(c_i(t) + c_k(t)) \frac{\sigma_{l-1}^{*2}(\mathbf{x})}{\theta_y} \right)}{\sigma_{l-1}^*(\mathbf{x})} \right\} \right. \\
& + E'_5 \Lambda_{52} \frac{\sigma_{l-1}^*(\mathbf{x})}{\sqrt{2\pi}} \exp \left(- \frac{\left((Y_{-L})_i - \mu_{l-1}^*(\mathbf{x}) - \sqrt{3}(c_i(t) + c_k(t)) \frac{\sigma_{l-1}^{*2}(\mathbf{x})}{\theta_y} \right)^2}{2\sigma_{l-1}^{*2}(\mathbf{x})} \right) \left. \right],
\end{aligned}$$

$$\Lambda_{11} = \begin{pmatrix} 1 \\ \mu_{l-1}^*(\mathbf{x}) - \frac{\sqrt{3}c_i(t)\sigma_{l-1}^{*2}(\mathbf{x})}{\theta_y} \end{pmatrix}, \Lambda_{12} = \begin{pmatrix} 0 \\ 1 \end{pmatrix}, \Lambda_{21} = \begin{pmatrix} 1 \\ -\mu_{l-1}^*(\mathbf{x}) - \frac{\sqrt{3}c_i(t)\sigma_{l-1}^{*2}(\mathbf{x})}{\theta_y} \end{pmatrix},$$

$$\Lambda_{31} = \begin{pmatrix} 1 \\ \mu_{l-1}^*(\mathbf{x}) - \frac{\sqrt{3}(c_i(t)+c_k(t))\sigma_{l-1}^{*2}(\mathbf{x})}{\theta_y} \\ \left(\mu_{l-1}^*(\mathbf{x}) - \frac{\sqrt{3}(c_i(t)+c_k(t))\sigma_{l-1}^{*2}(\mathbf{x})}{\theta_y} \right)^2 + \sigma_{l-1}^{*2}(\mathbf{x}) \end{pmatrix}, \Lambda_{32} = \begin{pmatrix} 0 \\ 1 \\ \mu_{l-1}^*(\mathbf{x}) - \frac{\sqrt{3}(c_i(t)+c_k(t))\sigma_{l-1}^{*2}(\mathbf{x})}{\theta_y} + (Y_{-L})_k \end{pmatrix},$$

$$\Lambda_{41} = \begin{pmatrix} 1 \\ \mu_{l-1}^*(\mathbf{x}) \\ \left(\mu_{l-1}^*(\mathbf{x}) \right)^2 + \sigma_{l-1}^{*2}(\mathbf{x}) \end{pmatrix}, \Lambda_{42} = \begin{pmatrix} 0 \\ 1 \\ \mu_{l-1}^*(\mathbf{x}) + (Y_{-L})_i \end{pmatrix},$$

$$\Lambda_{43} = \begin{pmatrix} 0 \\ 1 \\ \mu_{l-1}^*(\mathbf{x}) + (Y_{-L})_k \end{pmatrix}, \Lambda_{51} = \begin{pmatrix} 1 \\ -\mu_{l-1}^*(\mathbf{x}) - \frac{\sqrt{3}(c_i(t)+c_k(t))\sigma_{l-1}^{*2}(\mathbf{x})}{\theta_y} \\ \left(\mu_{l-1}^*(\mathbf{x}) + \frac{\sqrt{3}(c_i(t)+c_k(t))\sigma_{l-1}^{*2}(\mathbf{x})}{\theta_y} \right)^2 + \sigma_{l-1}^{*2}(\mathbf{x}) \end{pmatrix},$$

$$\begin{aligned}
\Lambda_{52} &= \begin{pmatrix} 0 \\ 1 \\ -\mu_{l-1}^*(\mathbf{x}) - \frac{\sqrt{3}(c_i(t)+c_k(t))\sigma_{l-1}^{*2}(\mathbf{x})}{\theta_y} - (Y_{-L})_i \end{pmatrix}, E_1 = \frac{1}{\theta_y} \begin{pmatrix} \theta_y - \sqrt{3}c_i(t)(Y_{-L})_i \\ \sqrt{3}c_i(t) \end{pmatrix}, \\
E_2 &= \frac{1}{\theta_y} \begin{pmatrix} \theta_y + \sqrt{3}c_i(t)(Y_{-L})_i \\ \sqrt{3}c_i(t) \end{pmatrix}, \\
E_3 &= \frac{1}{\theta_y^2} \begin{pmatrix} \theta_y^2 + 3c_i(t)c_k(t)(Y_{-L})_i(Y_{-L})_k - \sqrt{3}\theta_y(c_i(t)(Y_{-L})_i + c_k(t)(Y_{-L})_k) \\ \sqrt{3}(c_i(t) + c_k(t))\theta_y - 3c_i(t)c_k(t)((Y_{-L})_i + (Y_{-L})_k) \\ 3c_i(t)c_k(t) \end{pmatrix}, \\
E_4 &= \frac{1}{\theta_y^2} \begin{pmatrix} \theta_y^2 - 3c_i(t)c_k(t)(Y_{-L})_i(Y_{-L})_k + \sqrt{3}\theta_y(c_k(t)(Y_{-L})_k - c_i(t)(Y_{-L})_i) \\ \sqrt{3}(c_i(t) - c_k(t))\theta_y + 3c_i(t)c_k(t)((Y_{-L})_i + (Y_{-L})_k) \\ -3c_i(t)c_k(t) \end{pmatrix}, \\
E_5 &= \frac{1}{\theta_y^2} \begin{pmatrix} \theta_y^2 + 3c_i(t)c_k(t)(Y_{-L})_i(Y_{-L})_k + \sqrt{3}\theta_y(c_i(t)(Y_{-L})_i + c_k(t)(Y_{-L})_k) \\ \sqrt{3}(c_i(t) + c_k(t))\theta_y + 3c_i(t)c_k(t)((Y_{-L})_i + (Y_{-L})_k) \\ 3c_i(t)c_k(t) \end{pmatrix},
\end{aligned}$$

for $(Y_{-L})_i \leq (Y_{-L})_k$. If $(Y_{-L})_i > (Y_{-L})_k$, interchange $(Y_{-L})_i$ and $(Y_{-L})_k$. Φ is the cumulative distribution function of a standard normal distribution.

S5.2 Matérn-2.5 kernel

For Matérn kernel with the smoothness parameter of 2.5, ξ_i and ζ_{ik} are provided as follows,

$$\begin{aligned}
\xi_i &= \exp \left(\frac{5c_i^2(t)\sigma_{l-1}^{*2}(\mathbf{x}) + 2\sqrt{5}c_i(t)\theta_y((Y_{-L})_i - \mu_{l-1}^*(\mathbf{x}))}{2\theta_y^2} \right) \\
&\times \left[E'_1 \Lambda_{11} \Phi \left(\frac{\mu_{l-1}^*(\mathbf{x}) - (Y_{-L})_i - \frac{\sqrt{5}c_i(t)\sigma_{l-1}^{*2}(\mathbf{x})}{\theta_y}}{\sigma_{l-1}^*(\mathbf{x})} \right) \right. \\
&+ \left. E'_1 \Lambda_{12} \frac{\sigma_{l-1}^*(\mathbf{x})}{\sqrt{2\pi}} \exp \left(- \frac{\left((Y_{-L})_i - \mu_{l-1}^*(\mathbf{x}) + \frac{\sqrt{5}c_i(t)\sigma_{l-1}^{*2}(\mathbf{x})}{\theta_y} \right)^2}{2\sigma_{l-1}^{*2}(\mathbf{x})} \right) \right] \\
&+ \exp \left(\frac{5c_i^2(t)\sigma_{l-1}^{*2}(\mathbf{x}) - 2\sqrt{5}c_i(t)\theta_y((Y_{-L})_i - \mu_{l-1}^*(\mathbf{x}))}{2\theta_y^2} \right) \\
&\times \left[E'_2 \Lambda_{21} \Phi \left(\frac{-\mu_{l-1}^*(\mathbf{x}) + (Y_{-L})_i - \frac{\sqrt{5}c_i(t)\sigma_{l-1}^{*2}(\mathbf{x})}{\theta_y}}{\sigma_{l-1}^*(\mathbf{x})} \right) \right. \\
&+ \left. E'_2 \Lambda_{22} \cdot \frac{\sigma_{l-1}^*(\mathbf{x})}{\sqrt{2\pi}} \exp \left(- \frac{\left((Y_{-L})_i - \mu_{l-1}^*(\mathbf{x}) - \frac{\sqrt{5}c_i(t)\sigma_{l-1}^{*2}(\mathbf{x})}{\theta_y} \right)^2}{2\sigma_{l-1}^{*2}(\mathbf{x})} \right) \right], \\
\zeta_{ik} &= \exp \left\{ \frac{5\sigma_{l-1}^{*2}(\mathbf{x})(c_i(t) + c_k(t))^2 + 2\sqrt{5}\theta_y (c_i(t)((Y_{-L})_i - \mu_{l-1}^*(\mathbf{x})) + c_k(t)((Y_{-L})_k - \mu_{l-1}^*(\mathbf{x})))}{2\theta_y^2} \right\} \\
&\times \left[E'_3 \Lambda_{31} \Phi \left\{ \frac{\left(\mu_{l-1}^*(\mathbf{x}) - (Y_{-L})_k - \sqrt{5}(c_i(t) + c_k(t)) \frac{\sigma_{l-1}^{*2}(\mathbf{x})}{\theta_y} \right)}{\sigma_{l-1}^*(\mathbf{x})} \right\} \right. \\
&+ \left. E'_3 \Lambda_{32} \frac{\sigma_{l-1}^*(\mathbf{x})}{\sqrt{2\pi}} \exp \left(- \frac{\left((Y_{-L})_k - \mu_{l-1}^*(\mathbf{x}) + \sqrt{5}(c_i(t) + c_k(t)) \frac{\sigma_{l-1}^{*2}(\mathbf{x})}{\theta_y} \right)^2}{2\sigma_{l-1}^{*2}(\mathbf{x})} \right) \right] \\
&+ \exp \left\{ \frac{5\sigma_{l-1}^{*2}(\mathbf{x})(c_i(t) - c_k(t))^2 + 2\sqrt{5}\theta_y (c_i(t)((Y_{-L})_i - \mu_{l-1}^*(\mathbf{x})) - c_k(t)((Y_{-L})_k - \mu_{l-1}^*(\mathbf{x})))}{2\theta_y^2} \right\}
\end{aligned}$$

$$\begin{aligned}
& \times \left[E'_4 \Lambda_{41} \left(\Phi \left\{ \frac{(Y_{-L})_k - \mu_{l-1}^*(\mathbf{x})}{\sigma_{l-1}^*(\mathbf{x})} \right\} - \Phi \left\{ \frac{(Y_{-L})_i - \mu_{l-1}^*(\mathbf{x})}{\sigma_{l-1}^*(\mathbf{x})} \right\} \right) \right. \\
& + E'_4 \Lambda_{42} \frac{\sigma_{l-1}^*(\mathbf{x})}{\sqrt{2\pi}} \exp \left(-\frac{((Y_{-L})_i - \mu_{l-1}^*(\mathbf{x}))^2}{2\sigma_{l-1}^{*2}(\mathbf{x})} \right) - E'_4 \Lambda_{43} \frac{\sigma_{l-1}^*(\mathbf{x})}{\sqrt{2\pi}} \exp \left(-\frac{((Y_{-L})_k - \mu_{l-1}^*(\mathbf{x}))^2}{2\sigma_{l-1}^{*2}(\mathbf{x})} \right) \left. \right] \\
& + \exp \left\{ \frac{5\sigma_{l-1}^{*2}(\mathbf{x})(c_i(t) + c_k(t))^2 - 2\sqrt{5}\theta_y (c_i(t)((Y_{-L})_i - \mu_{l-1}^*(\mathbf{x})) + c_k(t)((Y_{-L})_k - \mu_{l-1}^*(\mathbf{x})))}{2\theta_y^2} \right\} \\
& \times \left[E'_5 \Lambda_{51} \Phi \left\{ \frac{\left(-\mu_{l-1}^*(\mathbf{x}) + (Y_{-L})_i - \sqrt{5}(c_i(t) + c_k(t)) \frac{\sigma_{l-1}^{*2}(\mathbf{x})}{\theta_y} \right)}{\sigma_{l-1}^*(\mathbf{x})} \right\} \right. \\
& + E'_5 \Lambda_{52} \frac{\sigma_{l-1}^*(\mathbf{x})}{\sqrt{2\pi}} \exp \left(-\frac{\left((Y_{-L})_i - \mu_{l-1}^*(\mathbf{x}) - \sqrt{5}(c_i(t) + c_k(t)) \frac{\sigma_{l-1}^{*2}(\mathbf{x})}{\theta_y} \right)^2}{2\sigma_{l-1}^{*2}(\mathbf{x})} \right) \left. \right], \\
\Lambda_{11} &= \begin{pmatrix} 1 \\ \mu_{l-1}^*(\mathbf{x}) - \frac{\sqrt{5}c_i(t)\sigma_{l-1}^{*2}(\mathbf{x})}{\theta_y} \\ \left(\mu_{l-1}^*(\mathbf{x}) - \frac{\sqrt{5}c_i(t)\sigma_{l-1}^{*2}(\mathbf{x})}{\theta_y} \right)^2 + \sigma_{l-1}^{*2}(\mathbf{x}) \end{pmatrix}, \Lambda_{12} = \begin{pmatrix} 0 \\ 1 \\ \mu_{l-1}^*(\mathbf{x}) - \frac{\sqrt{5}c_i(t)\sigma_{l-1}^{*2}(\mathbf{x})}{\theta_y} + (Y_{-L})_i \end{pmatrix}, \\
\Lambda_{21} &= \begin{pmatrix} 1 \\ -\mu_{l-1}^*(\mathbf{x}) - \frac{\sqrt{5}c_i(t)\sigma_{l-1}^{*2}(\mathbf{x})}{\theta_y} \\ \left(\mu_{l-1}^*(\mathbf{x}) + \frac{\sqrt{5}c_i(t)\sigma_{l-1}^{*2}(\mathbf{x})}{\theta_y} \right)^2 + \sigma_{l-1}^{*2}(\mathbf{x}) \end{pmatrix}, \Lambda_{22} = \begin{pmatrix} 0 \\ 1 \\ -\mu_{l-1}^*(\mathbf{x}) - \frac{\sqrt{5}c_i(t)\sigma_{l-1}^{*2}(\mathbf{x})}{\theta_y} - (Y_{-L})_i \end{pmatrix}, \\
\Lambda_{31} &= \begin{pmatrix} 1 \\ \mu_c \\ \mu_c^2 + \sigma_{l-1}^{*2}(\mathbf{x}) \\ \mu_c (\mu_c^2 + 3\sigma_{l-1}^{*2}(\mathbf{x})) \\ \mu_c^4 + 6\mu_c^2\sigma_{l-1}^{*2}(\mathbf{x}) + 3\sigma_{l-1}^{*4}(\mathbf{x}) \end{pmatrix}, \mu_c = \mu_{l-1}^*(\mathbf{x}) - \sqrt{5}(c_i(t) + c_k(t)) \frac{\sigma_{l-1}^{*2}(\mathbf{x})}{\theta_y},
\end{aligned}$$

$$\begin{aligned}
\Lambda_{32} &= \begin{pmatrix} 0 \\ 1 \\ \mu_c + (Y_{-L})_k \\ \mu_c^2 + 2\sigma_{l-1}^{*2}(\mathbf{x}) + ((Y_{-L})_k)^2 + \mu_c(Y_{-L})_k \\ \mu_c^3 + ((Y_{-L})_k)^3 + (Y_{-L})_k\mu_c(\mu_c + (Y_{-L})_k) + \sigma_{l-1}^{*2}(\mathbf{x})(5\mu_c + 3(Y_{-L})_k) \end{pmatrix}, \\
\Lambda_{41} &= \begin{pmatrix} 1 \\ \mu^* \\ \mu^{*2} + \sigma_{l-1}^{*2}(\mathbf{x}) \\ \mu^*(\mu^{*2} + 3\sigma_{l-1}^{*2}(\mathbf{x})) \\ \mu^{*4} + 6\mu_c^2\sigma_{l-1}^{*2}(\mathbf{x}) + 3\sigma_{l-1}^{*4}(\mathbf{x}) \end{pmatrix}, \mu^* = \mu_{l-1}^*(\mathbf{x}), \\
\Lambda_{42} &= \begin{pmatrix} 0 \\ 1 \\ \mu^* + (Y_{-L})_i \\ \mu^{*2} + 2\sigma_{l-1}^{*2}(\mathbf{x}) + ((Y_{-L})_i)^2 + \mu^*(Y_{-L})_i \\ \mu^{*3} + ((Y_{-L})_i)^3 + (Y_{-L})_i\mu^*(\mu^* + (Y_{-L})_i) + \sigma_{l-1}^{*2}(\mathbf{x})(5\mu^* + 3(Y_{-L})_i) \end{pmatrix}, \\
\Lambda_{43} &= \begin{pmatrix} 0 \\ 1 \\ \mu^* + (Y_{-L})_k \\ \mu^{*2} + 2\sigma_{l-1}^{*2}(\mathbf{x}) + ((Y_{-L})_k)^2 + \mu^*(Y_{-L})_k \\ \mu^{*3} + ((Y_{-L})_k)^3 + (Y_{-L})_k\mu^*(\mu^* + (Y_{-L})_k) + \sigma_{l-1}^{*2}(\mathbf{x})(5\mu^* + 3(Y_{-L})_k) \end{pmatrix},
\end{aligned}$$

$$\Lambda_{51} = \begin{pmatrix} 1 \\ -\mu_d \\ \mu_d^2 + \sigma_{l-1}^{*2}(\mathbf{x}) \\ -\mu_d (\mu_d^2 + 3\sigma_{l-1}^{*2}(\mathbf{x})) \\ \mu_d^4 + 6\mu_d^2\sigma_{l-1}^{*2}(\mathbf{x}) + 3\sigma_{l-1}^{*4}(\mathbf{x}) \end{pmatrix}, \mu_d = \mu_{l-1}^*(\mathbf{x}) + \sqrt{5}(c_i(t) + c_k(t)) \frac{\sigma_{l-1}^{*2}(\mathbf{x})}{\theta_y},$$

$$\Lambda_{52} = \begin{pmatrix} 0 \\ 1 \\ -\mu_d - (Y_{-L})_i \\ \mu_d^2 + 2\sigma_{l-1}^{*2}(\mathbf{x}) + ((Y_{-L})_i)^2 + \mu_d(Y_{-L})_i \\ -\mu_d^3 - ((Y_{-L})_i)^3 - (Y_{-L})_i\mu_d(\mu_d + (Y_{-L})_i) - \sigma_{l-1}^{*2}(\mathbf{x})(5\mu_d + 3(Y_{-L})_i) \end{pmatrix},$$

$$E_1 = \frac{1}{3\theta_y^2} \begin{pmatrix} 3\theta_y^2 - 3\sqrt{5}c_i(t)\theta_y(Y_{-L})_i + 5c_i^2(t)((Y_{-L})_i)^2 \\ 3\sqrt{5}c_i(t)\theta_y - 10c_i^2(t)(Y_{-L})_i \\ 5c_i^2(t) \end{pmatrix},$$

$$E_2 = \frac{1}{3\theta_y^2} \begin{pmatrix} 3\theta_y^2 + 3\sqrt{5}c_i(t)\theta_y(Y_{-L})_i + 5c_i^2(t)((Y_{-L})_i)^2 \\ 3\sqrt{5}c_i(t)\theta_y + 10c_i^2(t)(Y_{-L})_i \\ 5c_i^2(t) \end{pmatrix},$$

$$E_3 = \frac{1}{9\theta_y^4} \begin{pmatrix} E_{31} & E_{32} & E_{33} & E_{34} & E_{35} \end{pmatrix}^\top,$$

$$\begin{aligned} E_{31} &= 9\theta_y^4 + 25c_i^2(t)c_k^2(t)((Y_{-L})_i)^2((Y_{-L})_k)^2 \\ &\quad - 3\sqrt{5}\theta_y(c_i(t)(Y_{-L})_i + c_k(t)(Y_{-L})_k)(3\theta_y^2 + 5c_i(t)c_k(t)(Y_{-L})_i(Y_{-L})_k) \\ &\quad + 15\theta_y^2(c_i^2(t)((Y_{-L})_i)^2 + c_k^2(t)((Y_{-L})_k)^2 + 3c_i(t)c_k(t)(Y_{-L})_i(Y_{-L})_k), \end{aligned}$$

$$\begin{aligned}
E_{32} &= 9\sqrt{5}(c_i(t) + c_k(t))\theta_y^3 + 15\sqrt{5}c_i(t)c_k(t)\theta_y (c_i(t) ((Y_{-L})_i)^2 + c_k(t) ((Y_{-L})_k)^2) \\
&\quad - 15\theta_y^2 (c_i(t)(Y_{-L})_i(2c_i(t) + 3c_k(t)) + c_k(t)(Y_{-L})_k(2c_k(t) + 3c_i(t))) \\
&\quad - 50c_i^2(t)c_k^2(t)(Y_{-L})_i(Y_{-L})_k ((Y_{-L})_i + (Y_{-L})_k) + 30\sqrt{5}c_i(t)c_k(t)(c_i(t) + c_k(t))\theta_y(Y_{-L})_i(Y_{-L})_k, \\
E_{33} &= 5 \{ 5c_i^2(t)c_k^2(t)((Y_{-L})_i)^2 + ((Y_{-L})_k)^2 + 4(Y_{-L})_i(Y_{-L})_k + 3(c_i^2(t) + c_k^2(t) + 3c_i(t)c_k(t))\theta_y^2 \\
&\quad - 3\sqrt{5}c_i(t)c_k(t)\theta_y (2c_i(t)(Y_{-L})_i + 2c_k(t)(Y_{-L})_k + c_k(t)(Y_{-L})_i + c_i(t)(Y_{-L})_k) \} \\
E_{34} &= 5 \left(3\sqrt{5}c_i(t)c_k(t)(c_i(t) + c_k(t))\theta_y - 10c_i^2(t)c_k^2(t)((Y_{-L})_i + (Y_{-L})_k) \right), E_{35} = 25c_i^2(t)c_k^2(t), \\
E_4 &= \frac{1}{9\theta_y^4} \begin{pmatrix} E_{41} & E_{42} & E_{43} & E_{44} & E_{45} \end{pmatrix}^\top, \\
E_{41} &= 9\theta_y^4 + 25c_i^2(t)c_k^2(t) ((Y_{-L})_i)^2 ((Y_{-L})_k)^2 \\
&\quad + 3\sqrt{5}\theta_y (c_k(t)(Y_{-L})_k - c_i(t)(Y_{-L})_i) (3\theta_y^2 - 5c_i(t)c_k(t)(Y_{-L})_i(Y_{-L})_k) \\
&\quad + 15\theta_y^2 (c_i^2(t) ((Y_{-L})_i)^2 + c_k^2(t) ((Y_{-L})_k)^2 - 3c_i(t)c_k(t)(Y_{-L})_i(Y_{-L})_k), \\
E_{42} &= 9\sqrt{5}(c_i(t) - c_k(t))\theta_y^3 + 15\sqrt{5}c_i(t)c_k(t)\theta_y (c_k(t) ((Y_{-L})_k)^2 - c_i(t) ((Y_{-L})_i)^2) \\
&\quad - 15\theta_y^2 (c_i(t)(Y_{-L})_i(2c_i(t) - 3c_k(t)) + c_k(t)(Y_{-L})_k(2c_k(t) - 3c_i(t))) \\
&\quad - 50c_i^2(t)c_k^2(t)(Y_{-L})_i(Y_{-L})_k ((Y_{-L})_i + (Y_{-L})_k) + 30\sqrt{5}c_i(t)c_k(t)(c_k(t) - c_i(t))\theta_y(Y_{-L})_i(Y_{-L})_k, \\
E_{43} &= 5 \{ 5c_i^2(t)c_k^2(t)((Y_{-L})_i)^2 + ((Y_{-L})_k)^2 + 4(Y_{-L})_i(Y_{-L})_k + 3(c_i^2(t) + c_k^2(t) - 3c_i(t)c_k(t))\theta_y^2 \\
&\quad - 3\sqrt{5}c_i(t)c_k(t)\theta_y (2c_k(t)(Y_{-L})_k - 2c_i(t)(Y_{-L})_i + c_k(t)(Y_{-L})_i - c_i(t)(Y_{-L})_k) \} \\
E_{44} &= 5 \left(3\sqrt{5}c_i(t)c_k(t)(c_k(t) - c_i(t))\theta_y - 10c_i^2(t)c_k^2(t)((Y_{-L})_i + (Y_{-L})_k) \right), E_{45} = 25c_i^2(t)c_k^2(t), \\
E_5 &= \frac{1}{9\theta_y^4} \begin{pmatrix} E_{51} & E_{52} & E_{53} & E_{54} & E_{55} \end{pmatrix}^\top, \\
E_{51} &= 9\theta_y^4 + 25c_i^2(t)c_k^2(t) ((Y_{-L})_i)^2 ((Y_{-L})_k)^2 \\
&\quad + 3\sqrt{5}\theta_y (c_i(t)(Y_{-L})_i + c_k(t)(Y_{-L})_k) (3\theta_y^2 + 5c_i(t)c_k(t)(Y_{-L})_i(Y_{-L})_k) \\
&\quad + 15\theta_y^2 (c_i^2(t) ((Y_{-L})_i)^2 + c_k^2(t) ((Y_{-L})_k)^2 + 3c_i(t)c_k(t)(Y_{-L})_i(Y_{-L})_k),
\end{aligned}$$

$$\begin{aligned}
E_{52} &= 9\sqrt{5}(c_i(t) + c_k(t))\theta_y^3 + 15\sqrt{5}c_i(t)c_k(t)\theta_y (c_i(t) ((Y_{-L})_i)^2 + c_k(t) ((Y_{-L})_k)^2) \\
&\quad + 15\theta_y^2 (c_i(t)(Y_{-L})_i(2c_i(t) + 3c_k(t)) + c_k(t)(Y_{-L})_k(2c_k(t) + 3c_i(t))) \\
&\quad + 50c_i^2(t)c_k^2(t)(Y_{-L})_i(Y_{-L})_k ((Y_{-L})_i + (Y_{-L})_k) + 30\sqrt{5}c_i(t)c_k(t)(c_i(t) + c_k(t))\theta_y(Y_{-L})_i(Y_{-L})_k, \\
E_{53} &= 5 \left\{ 5c_i^2(t)c_k^2(t)((Y_{-L})_i)^2 + ((Y_{-L})_k)^2 + 4(Y_{-L})_i(Y_{-L})_k + 3(c_i^2(t) + c_k^2(t) + 3c_i(t)c_k(t))\theta_y^2 \right. \\
&\quad \left. + 3\sqrt{5}c_i(t)c_k(t)\theta_y (2c_i(t)(Y_{-L})_i + 2c_k(t)(Y_{-L})_k + c_k(t)(Y_{-L})_i + c_i(t)(Y_{-L})_k) \right\} \\
E_{54} &= 5 \left(3\sqrt{5}c_i(t)c_k(t)(c_i(t) + c_k(t))\theta_y + 10c_i^2(t)c_k^2(t)((Y_{-L})_i + (Y_{-L})_k) \right), E_{55} = 25c_i^2(t)c_k^2(t),
\end{aligned}$$

for $(Y_{-L})_i \leq (Y_{-L})_k$. If $(Y_{-L})_i > (Y_{-L})_k$, interchange $(Y_{-L})_i$ and $(Y_{-L})_k$.

S6 Stochastic EM for non-nested DNA model

Let $Y_{-L}^{*(m)} = (\mathbf{y}_1[1 : n_2]^T, \tilde{\mathbf{y}}_1^{(m)}[1 : \tilde{n}_2]^T, \mathbf{y}_2[1 : n_3]^T, \tilde{\mathbf{y}}_2^{(m)}[1 : \tilde{n}_3]^T, \dots, \mathbf{y}_{L-1}[1 : n_L]^T)^T$, and denote $\mathbf{X}_{-1}^* = ((\mathcal{X}_2^*)^T, \dots, (\mathcal{X}_L^*)^T)^T$ as the combined inputs with corresponding tuning parameters $\mathbf{t}_{-1}^* = (t_2 \mathbf{1}_{n_2}^T, \dots, t_L \mathbf{1}_{n_L}^T)^T$. Here, n_l^* and \tilde{n}_l represents the sample sizes of the combined outputs $\mathbf{y}_l^{*(m)}$ and the pseudo outputs $\tilde{\mathbf{y}}_l^{(m)}$, respectively. Across levels $2, \dots, L$, we further define the total number of the combined observations as $N_{-1}^* = \sum_{l=2}^L n_l^*$ and the number of imputed pseudo observations as $\tilde{N}_{-1} = N_{-1}^* - N_{-1}$.

• Initialization:

- For each $l = 1, \dots, L - 1$, fit independent GPs to $(\mathcal{X}_l, \mathbf{y}_l)$ and use the posterior mean to initialize $\tilde{\mathbf{y}}_l^{(0)}$. Update the combined outputs as $\mathbf{y}_l^{*(0)} := \mathbf{y}_l \cup \tilde{\mathbf{y}}_l^{(0)}$.
- Estimate parameters $\hat{\varphi}^{(0)}$ using MLE with the pseudo-complete dataset $\{\{\mathbf{y}_l^{*(0)}\}_{l=1}^L, \{\mathcal{X}_l^*\}_{l=1}^L, \{t_l\}_{l=1}^L\}$.

- For $m = 1, \dots, M$:

– **Imputation Step:**

- * Sample $\tilde{\mathbf{y}}_1$ from the posterior distribution

$$p(\tilde{\mathbf{y}}_1 | \mathbf{y}_1; \hat{\alpha}_1, \hat{\tau}_1^2, \hat{\boldsymbol{\theta}}_1) \sim \mathcal{N} \left(\mu_1(\tilde{\mathcal{X}}_1), \hat{\tau}_1^2 (K_1(\tilde{\mathcal{X}}_1, \tilde{\mathcal{X}}_1) - \mathbf{k}_1(\tilde{\mathcal{X}}_1)^T \mathbf{K}_1^{-1} \mathbf{k}_1(\tilde{\mathcal{X}}_1)) \right),$$

where

$$\mu_1(\tilde{\mathcal{X}}_1) = \hat{\alpha}_1 \mathbf{1}_{\tilde{n}_1} + \mathbf{k}_1(\tilde{\mathcal{X}}_1)^T \mathbf{K}_1^{-1} (\mathbf{y}_1 - \hat{\alpha}_1 \mathbf{1}_{n_1}),$$

$\mathbf{k}_1(\tilde{\mathcal{X}}_1)$ is an $\tilde{n}_1 \times n_1$ matrix with elements $(\mathbf{k}_1(\tilde{\mathcal{X}}_1))_{i,j} = K_1((\tilde{\mathcal{X}}_1)_i, \mathbf{x}_j^{[1]})$, and $K_1(\tilde{\mathcal{X}}_1, \tilde{\mathcal{X}}_1)$ is an $\tilde{n}_1 \times \tilde{n}_1$ matrix with elements $(K_1(\tilde{\mathcal{X}}_1, \tilde{\mathcal{X}}_1))_{i,j} = K_1((\tilde{\mathcal{X}}_1)_i, (\tilde{\mathcal{X}}_1)_j)$.

- * Sample $\{\tilde{\mathbf{y}}_l^{(m)}\}_{l=2}^{L-1}$ from $p(\{\tilde{\mathbf{y}}_l\}_{l=2}^{L-1} | Y_{-1}; \hat{\boldsymbol{\varphi}}^{(m-1)}, Y_{-L}^{*(m-1)})$, which follows a normal distribution with with the mean

$$\hat{\alpha}^{(m-1)} \mathbf{1}_{\tilde{N}_{-1}} - \mathbf{B}^{(m-1)} (\mathbf{C}^{(m-1)})^{-1} (Y_{-1} - \hat{\alpha}^{(m-1)} \mathbf{1}_{N_{-1}})$$

and the covariance

$$\mathbf{A}^{(m-1)} - \mathbf{B}^{(m-1)} (\mathbf{C}^{(m-1)})^{-1} (\mathbf{B}^{(m-1)})^T.$$

Here, $\mathbf{A} \in \mathbb{R}^{\tilde{N}_{-1} \times \tilde{N}_{-1}}$ is defined as

$$\begin{aligned} \mathbf{A}_{ij}^{(m-1)} = & K(((\mathbf{t}_{-1}^* \setminus \mathbf{t}_{-1})_i, (\mathbf{X}_{-1}^* \setminus \mathbf{X}_{-1})_i, (Y_{-L}^{*(m-1)} \setminus Y_{-L}^{(m-1)})_i), \\ & ((\mathbf{t}_{-1}^* \setminus \mathbf{t}_{-1})_j, (\mathbf{X}_{-1}^* \setminus \mathbf{X}_{-1})_j, (Y_{-L}^{*(m-1)} \setminus Y_{-L}^{(m-1)})_j)), \end{aligned}$$

where \mathbf{t}_{-1} and $Y_{-L}^{(m-1)}$ represent the subset of \mathbf{t}_{-1}^* and $Y_{-L}^{*(m-1)}$ corresponding

to the indices of \mathbf{X}_{-1} . The matrix $\mathbf{B} \in \mathbb{R}^{\tilde{N}-1 \times N-1}$ is given by

$$\mathbf{B}_{ij}^{(m-1)} = K \left(((\mathbf{t}_{-1}^* \setminus \mathbf{t}_{-1})_i, (\mathbf{X}_{-1}^* \setminus \mathbf{X}_{-1})_i, (Y_{-L}^{*(m-1)} \setminus Y_{-L}^{(m-1)})_i), ((\mathbf{t}_{-1})_j, (\mathbf{X}_{-1})_j, (Y_{-L}^{(m-1)})_j) \right).$$

Similarly, the matrix $\mathbf{C}^{(m-1)} \in \mathbb{R}^{N-1 \times N-1}$ is defined as

$$\mathbf{C}_{ij}^{(m-1)} = K \left(((\mathbf{t}_{-1})_i, (\mathbf{X}_{-1})_i, (Y_{-L}^{(m-1)})_i), ((\mathbf{t}_{-1})_j, (\mathbf{X}_{-1})_j, (Y_{-L}^{(m-1)})_j) \right).$$

The hyperparameters of the kernel function K , namely $\boldsymbol{\theta}$, β and δ , are plugged in by their estimates from the previous iteration, $\hat{\boldsymbol{\theta}}^{(m-1)}$, $\hat{\beta}^{(m-1)}$ and $\hat{\delta}^{(m-1)}$.

- **Maximization Step:** Given the pseudo-complete data $\{\{\mathbf{y}_l^{*(m)}\}_{l=1}^L, \{\mathcal{X}_l^*\}_{l=1}^L, \{t_l\}_{l=1}^L\}$, update the parameter estimates $\hat{\boldsymbol{\varphi}}^{(m)}$ by maximizing the likelihood function, as described in Section 2.3.

S7 Supporting figures in Sections 4 and 5

This section provides the supporting tables and figures for Sections 4 and 5, including the comparison results in Section 4 (Figure S1, S2, S3, and S4), and the demonstration of the model predictions with confidence intervals for Poisson’s equation and the heat equation in Section 5 (Figure S5).

References

- Ming, D. and Guillas, S. (2021). Linked Gaussian process emulation for systems of computer models using Matérn kernels and adaptive design. *SIAM/ASA Journal on Uncertainty Quantification*, 9(4):1615–1642.

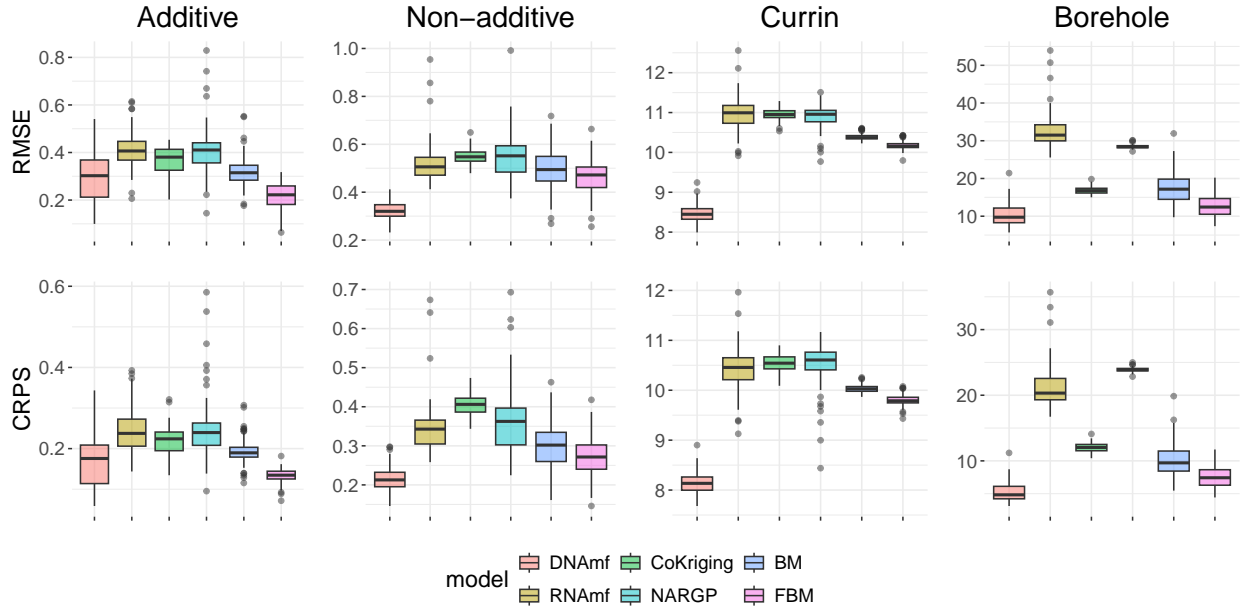


Figure S1: *RMSEs and CRPSs of four synthetic examples across 100 repetitions with $c = 0.75$ and $\gamma = 2$.*

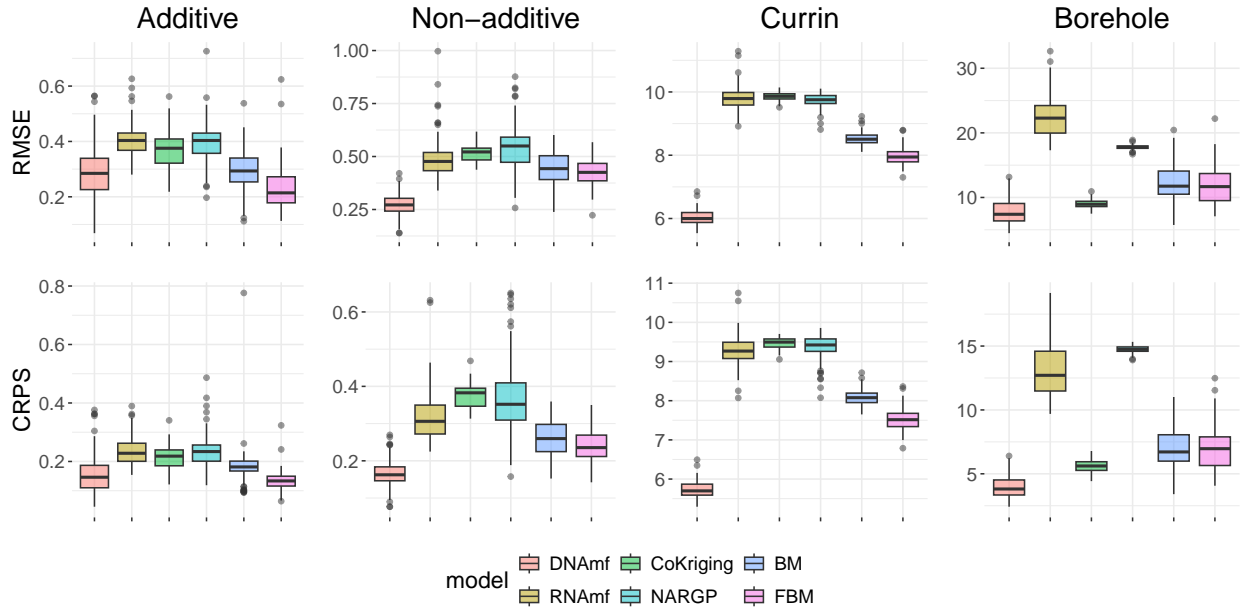


Figure S2: *RMSEs and CRPSs of four synthetic examples across 100 repetitions with $c = \frac{2}{3}$ and $\gamma = 1.5$.*

Schoenberg, I. J. (1938). Metric spaces and completely monotone functions. *Annals of Mathematics*, 39(4):811–841.

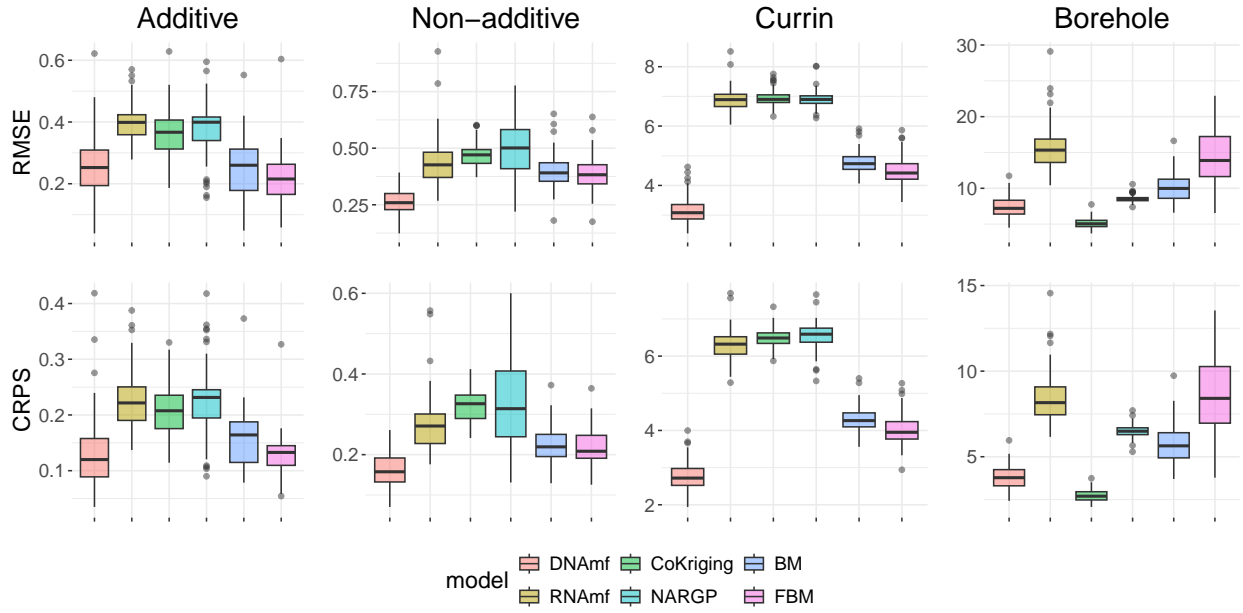


Figure S3: *RMSEs and CRPSs of four synthetic examples across 100 repetitions with $c = 0.55$ and $\gamma = 1$.*

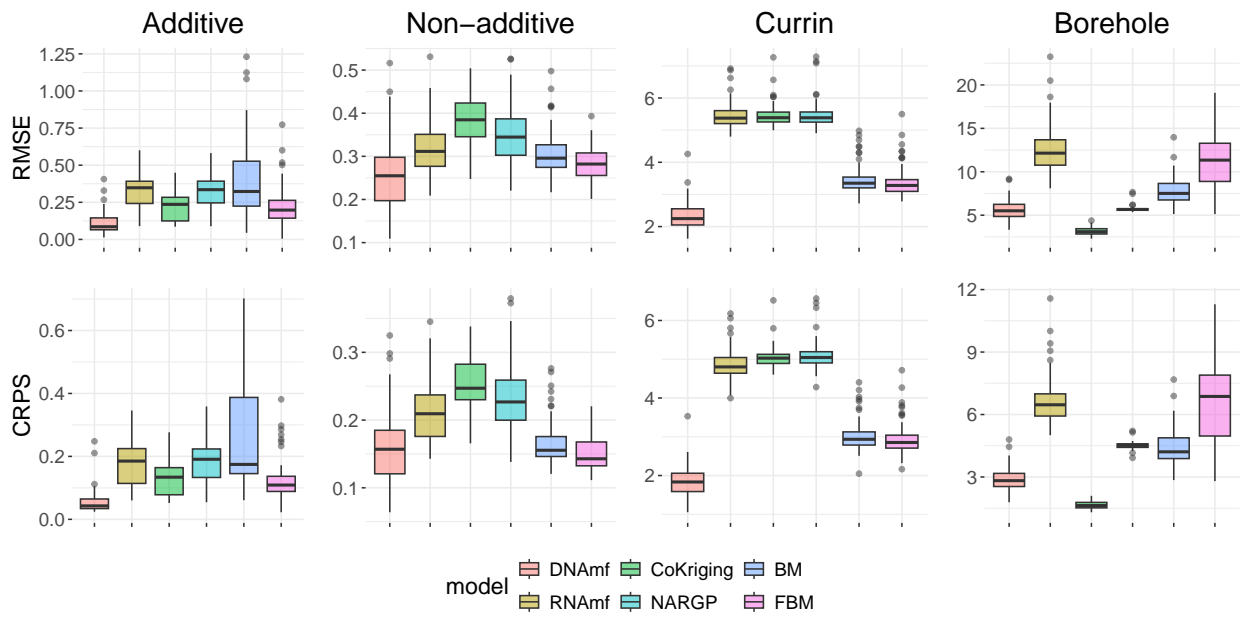


Figure S4: *RMSEs and CRPSs of four synthetic examples across 100 repetitions with $c = 0.5$ and $\gamma = 1$.*

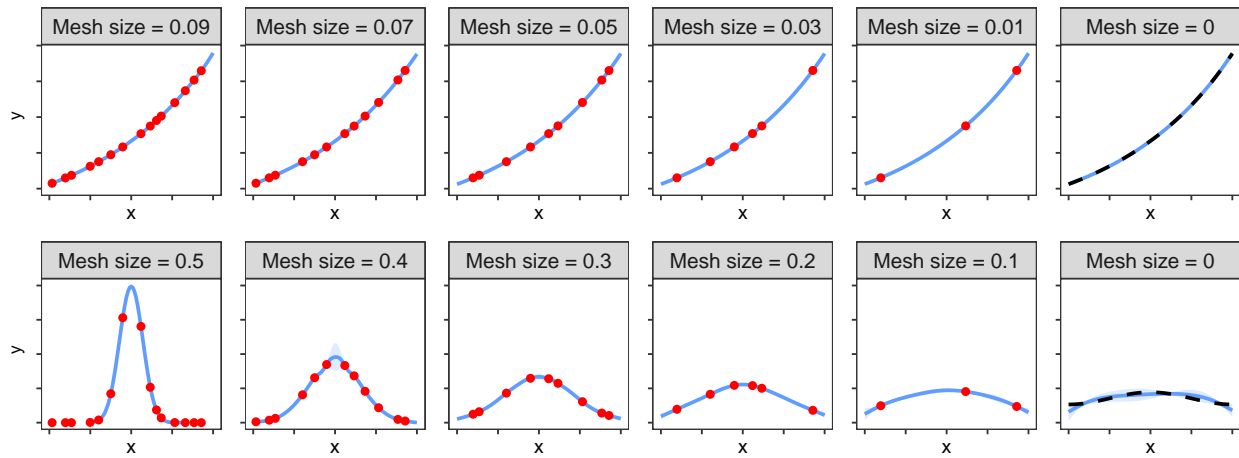


Figure S5: Illustrations of Poisson's equation (upper panel) and the heat equation (bottom panel) case studies. Each subplot represents subplots with tuning parameter values decreasing from large (left) to zero (right). In each subplot, the black dashed line represents the true function, red dots denote the design points, the blue line indicates the predicted function, and the shaded region depicts the 99% confidence interval.